Polarized light scattering measurements as a means to characterize particle size and composition of natural assemblages of marine particles

Daniel Koestner,* Dariusz Stramski, and Rick A. Reynolds

Marine Physical Laboratory, Scripps Institution of Oceanography, University of California San Diego, La Jolla, California 92093-0238, USA
*Corresponding author: dkoestne@ucsd.edu

Polarized light scattering measurements have the potential to provide improved characterization of natural particle assemblages in terms of particle size and composition. However, few studies have investigated this possibility for natural assemblages of marine particles. In this study, seawater samples representing contrasting assemblages of particles from coastal environments have been comprehensively characterized with measurements of angle-resolved polarized light scattering, particle size distribution, and particle composition. We observed robust trends linking samples containing higher proportions of large-sized particles with lower values of the maximum degree of linear polarization and the second element of the scattering matrix at a scattering angle of 100°, $p_{22}(100°)$. In contrast, lower values of $p_{22}(20°)$ were found in more non-phytoplankton—or inorganic–dominated samples. We also determined that three measurements involving the combinations of linearly polarized incident and scattered beams at two scattering angles (110° and 18°) have the potential to serve as useful proxies for estimating particle size and composition parameters. © 2020 Optical Society of America

https://doi.org/10.1364/AO.396709

1. INTRODUCTION

Light scattering by particles is foremost a function of particle size, shape, and composition, including internal structure. Light scattering also depends on light wavelength λ and varies with scattering angle ψ between the incident photon direction and scattered photon direction. Furthermore, particle scattering of polarized light exhibits additional complexity because of its dependence on the polarization state of incident light and the manner in which the particle can polarize or depolarize light through scattering. This light–particle interaction can be represented by a 4×4 scattering matrix, or Mueller matrix, which describes how a particle or ensemble of particles transforms the four-component Stokes vector of incident light into a four-component Stokes vector of scattered light [1]. Measurements of these polarized light scattering properties have the potential to advance characterization of marine particles.

The use of polarized light has been explored at length in astronomical and atmospheric sciences as it relates to the determination of particle composition and size distribution using measurements and theoretical modeling of aerosol particles [2–6]. This fundamental knowledge regarding the inherent polarized light scattering properties of aerosol particles has been paramount for the use of polarimetry in the retrieval of

atmospheric composition from satellite-based radiometric sensors [7]. The use of radiometric measurements of the ocean with polarimetric sensors, deployed either on *in situ*, airborne, or satellite platforms, also has the potential to complement traditional unpolarized radiometric measurements and improve characterization of particles suspended in seawater [8–10]. The current study aims primarily to improve understanding of the inherent polarization properties of light scattered by marine particles using measurements with a known artificial source of linearly polarized light beam.

In oceanography, the use of polarization in light scattering measurements of marine particles has been limited mainly to specific types of particles such as phytoplankton cultures [11–16] and mineral particles [4,14,17]. Although these studies have made measurements on well-characterized samples, the complexity and variability of natural particulate assemblages impose significant challenges for an understanding of bulk light scattering properties of seawater in terms of detailed particle size and compositional characteristics [18]. Measurements of inherent polarized light scattering properties of seawater samples containing natural assemblages of marine particles have been reported in few early studies, which have been generally

limited by the lack of ancillary characterization of seawater samples in terms of particle size distribution (PSD) and composition [19–21].

The current study focuses primarily on the three scattering matrix elements: $p_{11}(\psi, \lambda)$, $p_{12}(\psi, \lambda)$, and $p_{22}(\psi, \lambda)$. The degree of linear polarization of light scattered by particles, $\text{DoLP}_p(\psi, \lambda)$, describes the proportion of linearly polarized light relative to the total intensity of the scattered light beam. For various assemblages of particles, including suspended marine particles, and when the incident light beam is unpolarized, this quantity can be derived from $p_{11}(\psi, \lambda)$ and $p_{12}(\psi, \lambda)$, which require measurements involving linear polarization [14,22–24]. As early as 1930, it was observed that measurements of $\text{DoLP}_p(\psi, \lambda)$ on mineral particle suspensions at side scattering angles may be a useful indicator of average particle size [17]. A similar finding was observed with natural seawater samples in our recent study [25] in that the maximum value of $\text{DoLP}_p(\psi, \lambda)$ typically observed at scattering angles in the range $90°$–$100°$ was negatively correlated with a higher proportion of large-sized particles within natural assemblages of marine particles. In that study, 17 diverse seawater samples were examined, including ancillary characterization of PSD and organic versus inorganic particulate composition, but there was no determination of other polarized light scattering metrics such as $p_{22}(\psi, \lambda)$. Whereas $p_{12}(\psi, \lambda)$ essentially describes alterations between incident randomly polarized and scattered linearly polarized light, $p_{22}(\psi, \lambda)$ includes depolarization induced by the scattering medium via evaluation of co- and cross-polarization [1,22]. For marine particles, which are generally irregular in shape and internally inhomogeneous, the extent to which $p_{22}(\psi, \lambda)$ (after normalization to the first element of scattering matrix) differs, from 1 represents deviation from a collection of homogenous isotropic spheres [1,26]. Earlier measurements of $p_{22}(\psi, \lambda)$ for $\lambda = 488$ nm on seawater from a variety of western north-Atlantic and eastern north-Pacific waters indicate that $p_{22}(\psi, \lambda)$ decreases from ~ 1 at $\psi = 0°$ to a minimum of about 0.6–0.8 at $\psi \approx 100°$ [21], which is in general agreement with measurements by Kadyshevich [20] in Baltic waters. In these earlier studies, however, the role of different particle types in the variability of $\text{DoLP}_p(\psi, \lambda)$ and $p_{22}(\psi, \lambda)$ is unclear because particle assemblages were not characterized in terms of particle size and composition.

Given the continued increase in the applications of optical measurements in oceanography and recent technological advancements, further efforts to measure polarized light scattering by marine particles along with comprehensive characterization of particle assemblages in terms of size distribution and composition are warranted. One example of such recent advancements in technology is a commercial instrument capable of measuring $p_{11}(\psi, \lambda)$, $p_{12}(\psi, \lambda)$, and $p_{22}(\psi, \lambda)$ at a single light wavelength (e.g., $\lambda = 532$ nm) with high angular resolution (LISST-VSF; Sequoia Scientific). This instrument can be used both *in situ* and in benchtop laboratory configuration. Here we describe a study based on the use of the LISST-VSF instrument with a focus on angle-resolved polarized light scattering by marine particles. First, the scattering measurements of well-characterized seawater samples are described for the purpose of interpretation in terms of PSD and composition. Second, this study seeks to determine whether relatively simple optical relationships can be established to characterize size and compositional properties of marine particle assemblages as a function of polarized light scattering parameters at one or a few scattering angles.

2. METHODS

Table 1 defines a list of the important measurements and associated variables. The data presented here have been acquired using experimental procedures that are described in detail in our previous publications [25,27]. A short description of relevant methodology follows. More details related to particle-size fractionation and measurements of light absorption spectra, particle mass concentration, and PSD can be found in Koestner *et al.* [27], and details related to the LISST-VSF instrument, light scattering measurements, data processing, and Mie scattering calculations can be found in Koestner *et al.* [25]. Additional details of the LISST-VSF light scattering measurements and data processing are presented here, along with the development of an alternate correction function for improved estimates of the volume scattering function $\beta_p(\psi)$, degree of linear polarization $\text{DoLP}_p(\psi)$, and scattering matrix element $p_{22}(\psi)$ of particles suspended in seawater.

A. Water Samples

Sixteen seawater samples were collected in the region of San Diego, California, from June 2016 through March 2017. Two samples were collected at offshore locations aboard the R/V Sproul in mid-September 2016. One sample was collected 8 km offshore with Niskin bottles at a depth of 20 m coinciding with the measurement of maximum chlorophyll-a fluorescence. The other sample was collected 2 km offshore at a near-surface depth using the ship's surface seawater intake. Eleven near-shore samples were collected at the Scripps Institution of Oceanography (SIO) Pier. Three estuarine samples were collected 2 km inland in the San Diego River Estuary at different stages of high tide. The near-shore and estuarine samples were collected at a depth of about 0.5–1 m using either a bucket or a 5 L Niskin bottle. Note that one sample collected offshore near the Santa Barbara Channel, which was used in [25], has been removed from this analysis due to low particulate signal in LISST-VSF measurements.

Approximately 30–40 L of seawater were collected from a single location for each experiment with onshore laboratory analysis completed within 8 h after sampling, except for offshore samples, which were completed within 24 h after sampling. Before analysis, water was stored in 20 L carboys and protected from light. The water in the carboys was homogenized by gentle mixing immediately prior to removing samples for subsequent analysis. Special care was taken to ensure that subsamples of seawater used for different measurements and analyses were treated similarly and collected from carboys within 1 h of each other. All measurements were typically completed within a 4 h period.

Particle assemblage in each seawater sample was size fractionated using woven nylon or polyester mesh filters with pore sizes of 5 μm and 20 μm (Spectrum Labs). The details of the particle-size fractionation methodology are described in Ref. [27].

Table 1.   Measurement Symbols and Their Descriptions[a]

Symbol	Description [units]
ψ	Scattering angle with 0 defined as direction of initial propagation [deg]
$\perp$ or $\parallel$	Indicates polarization perpendicular or parallel to a reference plane
$\beta_p(\psi)$	Particulate volume scattering function [m^{-1} sr^{-1}] (Eq. (10))
$\beta_p^{\epsilon\epsilon}(\psi)$	Polarized light scattering by particles where $\epsilon = \perp$ or $\parallel$ [m^{-1} sr^{-1}]
$CF_f^{\epsilon\epsilon}(\psi)$	Correction functions for polarized light scattering combinations (Fig. 2)
$CF_f(\psi)$	Correction function for $\beta_p(\psi)$ from [25]
b_p	Particulate scattering coefficient [m^{-1}]; $2\pi \int_{0°}^{180°} \beta_p(\psi) \sin(\psi) \mathrm{d}\psi$
b_{bp}	Particulate backscattering coefficient [m^{-1}]; $2\pi \int_{90°}^{180°} \beta_p(\psi) \sin(\psi) \mathrm{d}\psi$
$\tilde{b}_{bp}$	Particulate backscattering ratio; b_{bp}/b_p
$DoLP_p(\psi)$	Degree of linear polarization of light scattered by particles (Eq. (11))
$DoLP_{p,max}$	Maximum value of $DoLP_p(\psi)$
ψ_{max}	Scattering angle of $DoLP_{p,max}$ [deg]
FWHM	The angular width of $DoLP_p(\psi)$ at half of $DoLP_{p,max}$ [deg]
$DoLP_p$ symmetry	Symmetry of $DoLP_p(\psi)$ about ψ_{max}; $DoLP_p(\psi_{max} - 45°)/DoLP_p(\psi_{max} + 45°)$
$p_{22}(\psi)$	Normalized scattering matrix element row 2 column 2 (Eq. (12))
$a_p(\lambda)$ and $a_{ph}(\lambda)$	Spectral absorption coefficients of particles and phytoplankton [m^{-1}]
SPM	Dry mass concentration of suspended particulate matter [g m^{-3}]
POC	Particulate organic carbon mass concentration [g m^{-3}]
Chla	Chlorophyll-a mass concentration [g m^{-3}]
PSD	Particle size distribution [number or volume concentration]
D_v^{50} and D_v^{90}	50th and 90th percentile diameter of the cumulative volume PSD [µm]

[a]All optical variables are at light wavelength $\lambda = 532$ nm in a vacuum unless otherwise stated.

B. Particle Characterization

The mass concentrations of suspended particulate matter (SPM), particulate organic carbon (POC), and chlorophyll-a (Chla) were determined with standard methodology following filtration of each original (i.e., unfractionated) seawater sample onto 25 mm Whatman glass fiber filters (GF/F) at low ($\leq$120 mm Hg) vacuum [28–30]. Ratios of these mass concentrations additionally serve as proxies of bulk compositional characteristics of the particulate assemblage, i.e., POC/SPM provides information about the contribution of organic versus inorganic particles and Chla/SPM about the contribution of phytoplankton to total particle mass concentration. For both the SPM and POC measurements, duplicate sample filters were collected, and the results were averaged to obtain the final estimates of SPM and POC for a given unfractionated seawater sample. Single sample filters were also collected to determine both SPM and POC for the 5 µm filtrate of all seawater samples with the exception of four samples from the SIO Pier. Single sample filters were collected and analyzed for Chla, and no determinations were made for the filtrates. Thus, there was a total of 16 measurements of Chla and 28 measurements of both POC and SPM available for analysis in conjunction with light scattering measurements.

The measurements of PSD were made using an electronic impedance method with a Multisizer 3 (Beckman Coulter) equipped with a 100 µm aperture, which allows particle counting in the size range of volume-equivalent spherical diameters D from 2 to 60 µm. Approximately 10 to 15 replicate measurements of 2 mL subsamples of each original (unfractionated) and two size-fractionated samples (i.e., the 5 µm and 20 µm filtrates) were collected. Assuming a spherical shape of particles, the particle volume distributions were determined from the particle number distributions for each sample, and the percentile-based particle diameters were calculated, such as the median diameter D_v^{50} and the 90th percentile diameter D_v^{90}, on the basis of particle volume distributions. These parameters have been shown to provide potentially useful metrics in the analysis of the relationships between the optical and particle size properties in seawater [31]. Of the 16 seawater samples collected for these experiments, two unfractionated samples from the SIO Pier, two 20 µm filtrate samples from the SIO Pier, and one 5 µm filtrate sample from the San Diego River Estuary were removed from further analysis because of uncertainty in the quality of Multisizer 3 measurements collected on these samples. Thus, there was a total of 43 measurements of PSD available for analysis in conjunction with light scattering measurements.

For the measurement of spectral absorption coefficient of particles $a_p(\lambda)$ [m^{-1}], original seawater samples were filtered onto 25 mm GF/F filters at low vacuum. The $a_p(\lambda)$ coefficient was determined in the spectral range from 300 to 850 nm at 1 nm intervals using a Lambda 18 UV/VIS spectrophotometer (Perkin Elmer) equipped with a 15 cm integrating sphere (RSA-PE-18, Labsphere) and with the filter placed inside the sphere [32,33]. Following the measurement of $a_p(\lambda)$, the methanol-treated filters were measured to determine the spectral absorption coefficient of non-algal particles [34], denoted as $a_d(\lambda)$. The spectral absorption coefficient of phytoplankton was then calculated as $a_{ph}(\lambda) = a_p(\lambda) - a_d(\lambda)$.

The correction of absorption measurements for path length amplification was made according to the recommendation in Ref. [33]. For this study, we evaluate the fraction $a_{ph}(\lambda)/a_p(\lambda)$ at $\lambda = 440$ nm for each original sample as an indication of the prevalence of phytoplankton in the sample. A total of

16 measurements of spectral absorption of samples was available for analysis in conjunction with light scattering measurements.

C. Brief Summary of Polarized Light Scattering Theory

For the incoherent elastic scattering of light at a given wavelength λ by a collection of particles suspended in water, the Stokes vector of incident light beam $S_i = [I_i\, Q_i\, U_i\, V_i]^T$ (where T represents the transpose operation) is transformed into the Stokes vector of scattered beam $S_s(\psi)$ by a scattering matrix $P(\psi)$. For an ensemble of randomly oriented particles exhibiting certain symmetry properties and no optical activity, the scattering matrix simplifies to six independent non-zero elements [1,23,35]:

$$S_s(\psi) = \begin{bmatrix} I_s(\psi) \\ Q_s(\psi) \\ U_s(\psi) \\ V_s(\psi) \end{bmatrix} = P(\psi)S_i$$

$$= C \begin{bmatrix} p_{11}(\psi) & p_{12}(\psi) & 0 & 0 \\ p_{12}(\psi) & p_{22}(\psi) & 0 & 0 \\ 0 & 0 & p_{33}(\psi) & p_{34}(\psi) \\ 0 & 0 & -p_{34}(\psi) & p_{44}(\psi) \end{bmatrix} \begin{bmatrix} I_i \\ Q_i \\ U_i \\ V_i \end{bmatrix},$$

$$\tag{1}$$

where λ has been omitted for brevity, C is a constant factor (for a given sample, light wavelength, and measurement geometry), and the reference plane is the scattering plane containing the incident and scattered directions. This form provides a reasonable description of the measured scattering matrix by suspensions of randomly oriented marine particles, including various specific types of particles present in seawater [4,11,14,21]. In the case of unpolarized incident light (i.e., Q_i, U_i, and V_i are all zero) the volume scattering function $\beta(\psi)$ equals (to within a constant factor) $p_{11}(\psi)$, and the degree of linear polarization $\mathrm{DoLP}(\psi)$ can be determined from [14,24,36]

$$\mathrm{DoLP}(\psi) = \frac{-p_{12}(\psi)}{p_{11}(\psi)}. \tag{2}$$

Note that the subscript p is not included here, as this is a general equation that can refer to the whole seawater sample with scattering contributions associated with both molecules and particles. Positive values of $\mathrm{DoLP}(\psi)$ are for dominantly perpendicular polarization, and negative values are for dominantly parallel polarization of scattered light. This definition of $\mathrm{DoLP}(\psi)$ has been widely used for characterizing the inherent scattering properties of various types of particles beyond aquatic particles, such as aerosol particles and cosmic dust [2,6].

D. LISST-VSF Instrument

Measurements with the LISST-VSF instrument (described in detail in Ref. [25]) consist of two scans of a 15 cm path within the sample, each with a different linear polarization state of the incident beam, i.e., parallel and perpendicular to a reference plane. For the LISST-VSF instrument geometry, parallel and perpendicular components of the incident beam are not with reference to the scattering plane, such that perpendicular and parallel components are not equivalent to the vertical and horizontal components in the scattering plane [37]. In this study, our interest is in scattered intensity measured from 14° to 155° with 1° interval using a roving eyeball sensor equipped with two photomultiplier tubes (PMTs) to detect parallel and perpendicularly polarized scattered light. The four measurement configurations allow for the determination of relative values of $p_{11}(\psi)$, $p_{12}(\psi)$, and $p_{22}(\psi)$. A baseline measurement of 0.2 μm filtered water, or seawater, was collected with LISST-VSF and subtracted from the sample measurements so that these scattering matrix elements refer to light scattered by suspended particles.

The four LISST-VSF measurement combinations [37] are

$$I_s^{\perp\|}(\psi) = p_{11}(\psi) - p_{12}(\psi) + \cos 2\psi(p_{12}(\psi) - p_{22}(\psi)),$$
$$\tag{3a}$$

$$I_s^{\perp\perp}(\psi) = \frac{1}{\alpha}[p_{11}(\psi) - p_{12}(\psi) - \cos 2\psi(p_{12}(\psi) - p_{22}(\psi))],$$
$$\tag{3b}$$

$$I_s^{\|\|}(\psi) = p_{11}(\psi) + p_{12}(\psi) + \cos 2\psi(p_{12}(\psi) + p_{22}(\psi)),$$
$$\tag{3c}$$

$$I_s^{\|\perp}(\psi) = \frac{1}{\alpha}[p_{11}(\psi) + p_{12}(\psi) - \cos 2\psi(p_{12}(\psi) + p_{22}(\psi))],$$
$$\tag{3d}$$

where the measured scattered intensity (component I_s of the scattered Stokes vector) is described with the first superscript character denoting the polarization state of the incident laser beam and the second superscript character denoting the polarization state of detected scattered light. For example, $I_s^{\perp\|}$ indicates that the incident laser is perpendicularly polarized and the detector is observing parallel polarized scattered light. Note that to arrive at Eq. (3) from Eq. (1), a rotation matrix must be included to account for the rotation of the scattered ray's polarization axes within the roving eyeball sensor [37]. The gain of the second PMT detector, observing only perpendicular light, relative to the first PMT detector, observing only parallel light, is described by the alpha factor α. These equations can be used to solve for $p_{11}(\psi)$, $p_{12}(\psi)$, and $p_{22}(\psi)$. It was previously determined from measurements with polystyrene bead suspensions that α was relatively constant throughout our experiments and can be treated as a constant for all measurements ($\alpha = 0.9335$, coefficient of variation <5% over 18 months throughout the period of experiments) [25].

E. Development of Alternate Correction Functions for LISST-VSF

In Ref. [25], it was found that independent corrections were needed for $\beta_p(\psi)$ and $\mathrm{DoLP}_p(\psi)$ following comparisons of measurements on nearly monodisperse polystyrene bead suspensions with simulations using Mie scattering theory for homogenous spheres. Six polystyrene bead diameters were used ranging from 100 nm to 2 μm in diameter. Koestner et al.'s [25] corrections included independent corrections for both $\beta_p(\psi)$ and $\mathrm{DoLP}_p(\psi)$, which were determined with the four

polarization measurement combinations [Eq. (3)]. These corrections, however, provide no correction for $p_{22}(\psi)$ or for the individual polarization measurement combinations. For the study presented here, reference values for each measurement combination were determined using Eq. (3) and $p_{11}^{\mathrm{Mie}}(\psi)$ and $p_{12}^{\mathrm{Mie}}(\psi)$ from Mie scattering calculations described in Ref. [25] while noting that $p_{22}(\psi) = p_{11}(\psi)$ for isotropic homogenous spheres [1,26,38]. For example, using perpendicularly polarized incident laser beam and parallel polarized detected light [Eq. (3a)],

$$\hat{I}_s^{\perp\|}(\psi) = p_{11}^{\mathrm{Mie}}(\psi) - p_{12}^{\mathrm{Mie}}(\psi) + \cos 2\psi (p_{12}^{\mathrm{Mie}}(\psi) - p_{11}^{\mathrm{Mie}}(\psi)),$$

$$\textbf{(4)}$$

$$\hat{\beta}_p^{\perp\|}(\psi) = \hat{I}_s^{\perp\|}(\psi) b_p^{\mathrm{REF}}, \qquad \textbf{(5)}$$

where the hat symbol denotes the reference value of polarized intensities determined from Mie scattering calculations and the reference value of particulate scattering coefficient b_p^{REF} was computed as described in Ref. [25]. For comparison of reference values with measured data from the LISST-VSF roving eyeball sensor, a scaling factor S_f must be included to convert the measured PMT counts into absolute units, i.e.,

$$\beta_p^{\perp\|*}(\psi) = S_f I_s^{\perp\|*}(\psi),$$

$$\beta_p^{\|\|*}(\psi) = S_f I_s^{\|\|*}(\psi), \qquad \textbf{(6)}$$

and, when appropriate, the relative gain factor α:

$$\beta_p^{\perp\perp*}(\psi) = \alpha S_f I_s^{\perp\perp*}(\psi),$$

$$\beta_p^{\|\perp*}(\psi) = \alpha S_f I_s^{\|\perp*}(\psi), \qquad \textbf{(7)}$$

where the asterisk denotes measured and uncorrected data from the LISST-VSF roving eyeball sensor.

Figure 1 shows the comparison of reference values and uncorrected measurements from the LISST-VSF for the four measurement combinations for 200 nm polystyrene beads (data processing version June 2012). There is disagreement in both shape and magnitude, which indicates that corrections are necessary. The four correction functions for each incident laser and detector polarization combination are defined as

$$\mathrm{CF}^{\perp\|}(\psi) = \frac{\hat{\beta}_p^{\perp\|}(\psi)}{\beta_p^{\perp\|*}(\psi)},$$

$$\mathrm{CF}^{\perp\perp}(\psi) = \frac{\hat{\beta}_p^{\perp\perp}(\psi)}{\beta_p^{\perp\perp*}(\psi)},$$

$$\mathrm{CF}^{\|\|}(\psi) = \frac{\hat{\beta}_p^{\|\|}(\psi)}{\beta_p^{\|\|*}(\psi)},$$

$$\mathrm{CF}^{\|\perp}(\psi) = \frac{\hat{\beta}_p^{\|\perp}(\psi)}{\beta_p^{\|\perp*}(\psi)}, \qquad \textbf{(8)}$$

The above calculations were performed for all bead sizes and concentrations described in Ref. [25]. The final correction functions (with subscript f) were determined identically to
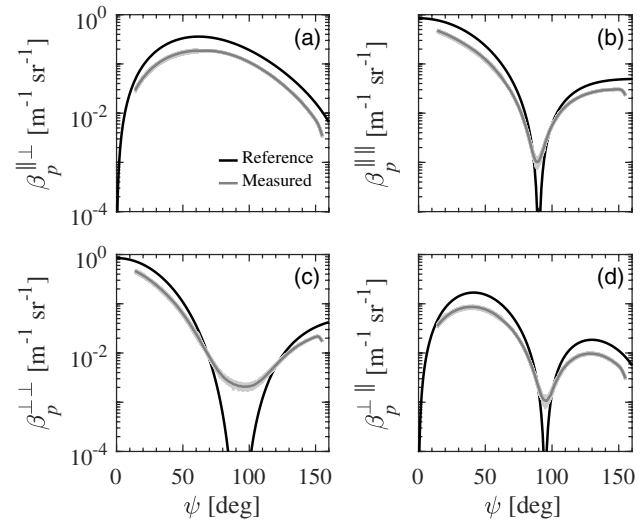

Fig. 1. Reference values (black) and measurements (gray) of the four polarized light scattering measurement combinations from the LISST-VSF for 200 nm diameter polystyrene beads suspended in water. The expected reference values obtained from Mie scattering calculations are plotted from 0.09° to 160° and measured values obtained with the LISST-VSF are plotted from 16° to 155°, both with linear scaling of the x axis. Quality controlled but uncorrected replicate measurements obtained with the LISST-VSF (light gray lines, $N = 128$) and the median value (dark gray line) are shown.

how the final correction function $\mathrm{CF}_f(\psi)$ for $\beta_p^{\mathrm{LISST}*}(\psi)$ in Ref. [25] was determined with 100, 200, and 400 nm beads, except that $\mathrm{CF}_f^{\perp\|}(\psi)$, $\mathrm{CF}_f^{\|\|}(\psi)$, and $\mathrm{CF}_f^{\perp\|}(\psi)$ within the range 85°–100° were set to their respective values at $\psi = 85°$ due to reference values near 0 around these angles [Figs. 1(b)–1(d)]. The reference values in this angular range are also sensitive to input PSD, complex refractive index, and assumptions of particle shape used in the Mie calculations for polystyrene bead suspensions, and measured data in this range were subject to low signal [Figs. 1(b)–1(d)]. As explained in Ref. [25], the larger beads (500 nm, 700 nm, and 2 µm) are not used in development of correction functions because the angular scattering pattern of these particles includes multiple, often sharp, interference maxima and minima, which render the comparison of measured and reference values particularly sensitive to even small uncertainties in theoretical calculations of reference values and possibly also in measured values due to finite angular resolution for any nominal measured angle. In particular, it is likely that significant uncertainties in the Mie calculations of exact magnitude of the maxima and minima of reference values can result from assumptions about PSD, refractive index, and perfect sphericity of polystyrene beads.

Differences between the correction functions determined separately with 100, 200, and 400 nm beads are within ±5% of the final $\mathrm{CF}_f^{\epsilon\epsilon}(\psi)$ for all relevant scattering angles with the exception of angular feature around 80° for the 400 nm beads, which is not included in the correction function because of the expected increase in uncertainty of the calculations of reference values [25]. The final correction functions are multiplied by the LISST-VSF roving eyeball measurements to produce corrected results, i.e.,

$$\beta_p^{\perp\parallel}(\psi) = \text{CF}^{\perp\parallel}(\psi)\beta_p^{\perp\parallel*}(\psi),$$

$$\beta_p^{\perp\perp}(\psi) = \text{CF}^{\perp\perp}(\psi)\beta_p^{\perp\perp*}(\psi),$$

$$\beta_p^{\parallel\parallel}(\psi) = \text{CF}^{\parallel\parallel}(\psi)\beta_p^{\parallel\parallel*}(\psi),$$

$$\beta_p^{\parallel\perp}(\psi) = \text{CF}^{\parallel\perp}(\psi)\beta_p^{\parallel\perp*}(\psi), \tag{9}$$

where the symbols on the left-hand side of the equations without the asterisk indicate that the measurements have been corrected. With these corrected measurement combinations, the final results of $\beta_p(\psi)$, $\text{DoLP}_p(\psi)$, and $p_{22}(\psi)$ are determined by rearranging Eq. (3) after utilizing Eqs. (6), (7), and (9). The final solutions are

$$\beta_p(\psi) = \frac{1}{4}[\beta_p^{\perp\parallel}(\psi) + \beta_p^{\parallel\parallel}(\psi) + \beta_p^{\perp\perp}(\psi) + \beta_p^{\parallel\perp}(\psi)], \tag{10}$$

$$\text{DoLP}_p(\psi) = \frac{\frac{1}{4}[\beta_p^{\parallel\perp}(\psi) + \beta_p^{\parallel\parallel}(\psi) - (\beta_p^{\perp\parallel}(\psi) + \beta_p^{\perp\perp}(\psi))]}{\beta_p(\psi)}, \tag{11}$$

$$p_{22}(\psi) = \frac{2\beta_p(\psi) - [(\beta_p^{\perp\parallel}(\psi) + \beta_p^{\perp\parallel}(\psi)\cos 2\psi)) + (\beta_p^{\parallel\parallel}(\psi) - \beta_p^{\parallel\parallel}(\psi)\cos(2\psi))]}{2\cos^2(2\psi)\beta_p(\psi)}, \tag{12a}$$

$$p_{22}(\psi) = \frac{2\beta_p(\psi) - [(\beta_p^{\parallel\perp}(\psi) + \beta_p^{\parallel\perp}(\psi)\cos(2\psi)) + (\beta_p^{\perp\perp}(\psi) - \beta_p^{\perp\perp}(\psi)\cos(2\psi))]}{2\cos^2(2\psi)\beta_p(\psi)}. \tag{12b}$$

Note that $p_{22}(\psi)$ is normalized by $\beta_p(\psi)$ here, as it is common notation when presenting results for scattering matrix elements [1,26,36]. We used the average results from Eqs. (12a) and (12b) for the final estimate of $p_{22}(\psi)$. The above solutions for $\beta_p(\psi)$, $\text{DoLP}_p(\psi)$, and $p_{22}(\psi)$ are provided in the LISST-VSF user manual and have been independently verified using Eq. (3); however, these derivations are not shown for brevity.

F. Application of Polarized Light Scattering Correction to Seawater Samples

In this study, all measurements of seawater samples with the LISST-VSF instrument were made in a laboratory benchtop configuration [25,27]. For each sample, between four and eight sequences of 50 replicate measurements were collected on the original (unfractionated) sample and two size-fractionated samples. During measurement a 5 cm magnetic stir bar was rotating at very low speed changing direction every 30 s, with additional gentle and random hand mixing of the sample done between sequences. Given that each measurement takes approximately 4 s, the full characterization of light scattering including all replicate measurements took $\sim15-30$ min. We assume that the samples did not undergo any significant physical, biological, or chemical changes over the period of data acquisition, and the total volumes interrogated ranged between $\sim20-120$ mL depending on scattering angle [27]. Measurements were made on samples satisfying the single scattering regime for LISST-VSF geometry with a particulate attenuation coefficient less than 2.5 m^{-1} [25]. In a few cases, dilutions were made to satisfy the single scattering requirement, and these dilutions were accounted for in light scattering results.

The correction functions developed above were applied to the four incident and detector polarization combinations [Eq. (9)] to determine $\beta_p^{\perp\parallel}(\psi)$, $\beta_p^{\parallel\parallel}(\psi)$, $\beta_p^{\perp\perp}(\psi)$, and $\beta_p^{\parallel\perp}(\psi)$ so that $\beta_p(\psi)$, $\text{DoLP}_p(\psi)$, and $p_{22}(\psi)$ could be computed for each measurement [following Eqs. (10), (11), and (12)]. We recall that $p_{22}(\psi)$ refers to the scattering matrix element associated with scattering by particles although in this case the subscript "p" is omitted for brevity. The determinations of final $\beta_p(\psi)$, $\text{DoLP}_p(\psi)$, and $p_{22}(\psi)$ involved quality control of about 200–400 replicate measurements, removing outliers potentially affected by measurement artifacts, deriving the median value at each angle from the remaining accepted measurements, and then smoothing the data three times with 3°, 3°, and 5° moving averages along the scattering angle axis. We used many replicate measurements for a given seawater sample to obtain median values of scattering parameters, which are representative of entire assemblages of particles and are of most relevance when comparing with other bulk particulate properties. Specifically, we found that the use of 50–100 replicates was sufficient to generate stable values of representative median scattering parameters of seawater samples, and for our samples we used even more replicates in the range 200–400 to achieve robust results.

Of the 16 seawater samples collected for these experiments, one original (unfractionated) sample and one 5 μm filtrate sample, both from the SIO Pier, were removed from further analysis because of LISST-VSF measurement artefacts identified during processing, which rendered all measurements collected on these samples erroneous. Thus, there was a total of 46 final functions of $\beta_p(\psi)$, $\text{DoLP}_p(\psi)$, and $p_{22}(\psi)$ available for analysis. Of these, 41 samples included acceptable PSD measurements, 27 included acceptable POC and SPM measurements, and 15 included acceptable spectral absorption and Chla measurements.

Table 1 includes the description of variables derived using the final $\beta_p(\psi)$ and $\text{DoLP}_p(\psi)$ measurements. The final $\beta_p(\psi)$ functions were used to estimate the particulate scattering and backscattering coefficients, b_p and b_{bp}, following the methodology described in Ref. [25]. These particulate scattering and backscattering coefficients were used to estimate the particulate backscattering ratio $\tilde{b}_{bp} = b_{bp}/b_p$. The final $\text{DoLP}_p(\psi)$ functions were used to derive several parameters used in our analysis: $\text{DoLP}_{p,\max}$, $\psi_{\max}$, full width at half-maximum (FWHM), and DoLP_p symmetry (Table 1). DoLP_p symmetry parameterizes symmetry of $\text{DoLP}_p(\psi)$ about its maximum value, typically observed at scattering angles near 90°. We evaluate this symmetry by comparing values of $\text{DoLP}_p(\psi)$ at $\psi = \psi_{\max} \pm 45°$, assuming that a symmetric $\text{DoLP}_p(\psi)$ shape would have approximately equivalent values at these scattering angles.

G. Relationships Between Scattering Parameters and Particle Characteristics

In Sections 3.C and 3.D we describe optically based relationships for estimating particle characteristics, specifically particle size parameter D_v^{90} and composition parameter POC/SPM, from optical parameters associated with the four polarized light scattering measurements: $\beta_p^{\perp\|}(\psi)$, $\beta_p^{\|\|}(\psi)$, $\beta_p^{\perp\perp}(\psi)$, and $\beta_p^{\|\perp}(\psi)$. These predictive relationships were determined from type II geometric mean linear regression analysis [39] between optical (assumed here as the independent variable) and particulate size or composition parameters (the dependent variable) measured on the natural seawater samples described earlier. Although type I linear regression analysis is typically used for establishing predictive relationships, type II regressions can be advantageous in some situations, especially when both the independent and dependent variables are subject to measurement uncertainty [39,40]. We examined both type I and type II regressions and compared several statistical parameters characterizing the differences between the model-predicted and measured values for both regression types. This analysis supported the notion that the predictive relationships determined from type II regression analysis are superior for our data. Specifically, the analysis of Bland–Altman plots [41,42] indicated that type II regressions produced no trends in the difference between model-predicted and observed values as a function of the average value, while type I regression did produce significant trends (not shown).

For the development of the optically based predictive relationships, the linear, exponential, and power function fits were obtained from a type II linear regression analysis for different sets of dependent (particle) versus independent (optical) variables. For the exponential fits, the dependent variable was log-transformed, and for the power function fits both the dependent and independent variables were log-transformed. All regressions were evaluated based on model-performance statistical variables described in Table 2 as well as the slope and y intercept determined from a type II linear regression of the model-predicted versus observed values. Pearson correlation coefficients were evaluated using log-transformed variables when applicable. Generally speaking, the random error was evaluated using root mean square deviation (RMSD) and MdAPD, while bias was evaluated using MdR and MB_{log} (Table 2). The comparative analysis of these statistics allowed selection of final best-performing relationship for each set of dependent versus independent variables, and these final relationships are presented in this paper.

Section 3.D seeks to identify simple optical proxies utilizing $\beta_p^{\perp\|}(\psi)$, $\beta_p^{\|\|}(\psi)$, $\beta_p^{\perp\perp}(\psi)$, and $\beta_p^{\|\perp}(\psi)$ at only one or two scattering angles. Ratio combinations at a single scattering angle were evaluated as proxies for D_v^{90}. The four polarized measurement combinations from the LISST-VSF instrument result in six unique ratio combinations, e.g., $\beta_p^{\|\|}(\psi_1)/\beta_p^{\|\|}(\psi_1)$. The subscript 1 is used here to emphasize that both the numerator and denominator use the same scattering angle ψ_1. For 41 samples that contain suitable LISST-VSF measurements and PSD measurements, a relationship of D_v^{90} versus each of the six scattering ratio combinations was evaluated at various angles ψ_1 between 20° and 120°. A total of 606 linear, exponential,

Table 2. Statistical Symbols and Their Descriptions

Symbol	Description
N	Number of samples
x_i or y_i	Measured value for sample i of N
$\bar{x}$ or $\bar{y}$	Mean value; $\bar{x} = \frac{1}{N}\sum_{i=1}^{N} x_i$, and likewise for $\bar{y}$
P_i or O_i	Model-predicted or observed value for sample i of N
R	Pearson correlation coefficient; $\frac{\sum_{i=1}^{N}(x_i-\bar{x})(y_i-\bar{y})}{\sqrt{\sum_{i=1}^{N}(x_i-\bar{x})^2}\sqrt{\sum_{i=1}^{N}(y_i-\bar{y})^2}}$
ρ	Spearman correlation coefficient; calculated as R with numerical rank values
Model-performance variables	
RMSD	Root mean square deviation; $\sqrt{\frac{1}{N}\sum_{i=1}^{N}(P_i-O_i)^2}$
MdAPD	Median absolute percent difference; 50th percentile of $\left|\frac{P_i-O_i}{O_i}\right| \times 100\%$
MdR	Median ratio; 50th percentile of $\frac{P_i}{O_i}$
MB_{log}	Mean bias of log-transformed data; $10^{N^{-1}\sum_{i=1}^{N}(\log P_i - \log O_i)}$

and power function relationships for D_v^{90} versus scattering parameters were examined, which resulted in the selection of final best-performing relationships presented in this paper.

The polarized light scattering ratios were also evaluated as proxies for POC/SPM, albeit with scattering angles varying independently in both the numerator and denominator, e.g., $\beta_p^{\|\perp}(\psi_1)/\beta_p^{\|\|}(\psi_2)$. In this case scattering angles were varied for ψ_1 in the range 80°–120° and ψ_2 in the range 16°–50°. By using these angular ranges we take advantage of information on polarized light scattering provided by LISST-VSF in both the forward and side/backward regions of the scattering angle. For 27 samples that contain suitable LISST-VSF measurements and POC/SPM measurements, a relationship of POC/SPM versus each scattering ratio combination was evaluated for every angle combination. A total of 1435 linear, exponential, and power function relationships for POC/SPM versus scattering parameters were examined for each scattering ratio combination, which resulted in the selection of final best-performing relationships presented in this paper.

3. RESULTS

A. Validation of Correction Functions

The new correction functions are validated by comparing final data products of $\beta_p(\psi)$, $DoLP_p(\psi)$, and $p_{22}(\psi)$ with reference results obtained from Mie scattering calculations for nearly monodisperse polystyrene bead suspensions. Note that the advantage of this new correction procedure compared to the Koestner *et al.* [25] corrections is there is only one set of correction functions, which together provide improved results for $\beta_p(\psi)$, $DoLP_p(\psi)$, the previously uncorrected $p_{22}(\psi)$, and four polarized light scattering measurement combinations. Figure 2 displays the final correction functions from Eq. (8): $CF_f^{\|\perp}(\psi)$, $CF_f^{\perp\perp}(\psi)$, $CF_f^{\|\|}(\psi)$, and $CF_f^{\perp\|}(\psi)$. For brevity, we also refer to these four correction functions as $CF_f^{\epsilon\epsilon}(\psi)$, where superscript $\epsilon\epsilon$ generally denotes polarized light scattering combinations, e.g., $\perp\|$ or $\|\|$. These correction functions are generally similar in magnitude to $CF_f(\psi)$ obtained in
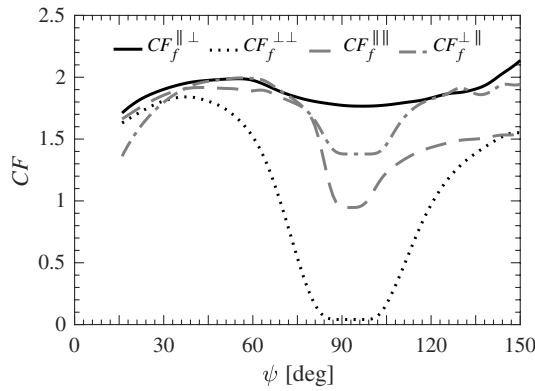
Fig. 2. Final correction functions $\mathrm{CF}_f^{\epsilon\epsilon}(\psi)$ for LISST-VSF measurements of each polarized light scattering measurement combination, as indicated in legend, over the angular range 16°–150° determined from analysis of 100, 200, and 400 nm polystyrene bead suspensions.
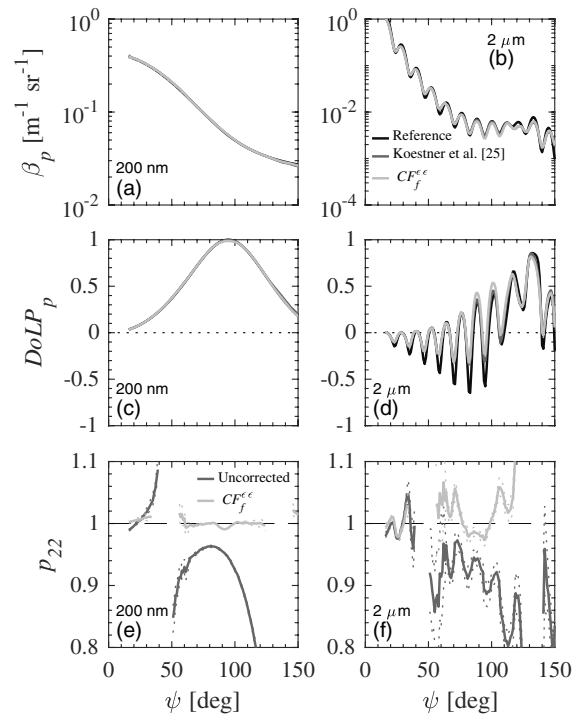

Fig. 3. Comparison of measurements obtained with two different corrections and reference values of (a), (b) $\beta_p(\psi)$, (c), (d) $\mathrm{DoLP}_p(\psi)$ and (e), (f) $p_{22}(\psi)$ for suspensions of polystyrene beads of (a), (c), (e) 200 nm and (b), (d), (e) 2 µm in diameter. Solid lines indicate median values while the dotted lines are 25th and 75th percentile values derived from replicate measurements. The legend in (b) is applicable to (a)–(d). The LISST-VSF measurement results obtained following corrections described in Ref. [25] are shown in dark gray and results obtained following the present correction $\mathrm{CF}_f^{\epsilon\epsilon}(\psi)$ are shown in light gray. The legend in (e) is applicable to (e), (f). A dashed line is shown in (e), (f) at 1 to indicate the expected reference value for polystyrene beads.

Ref. [25] with some noteworthy differences related to the use of linearly polarized light and the lack of polarized scattering data for $\psi < 16°$. $\mathrm{CF}_f^{\parallel\perp}(\psi)$ is most similar to $\mathrm{CF}_f(\psi)$ in shape and magnitude, varying within a relatively narrow range of values between about 1.7 at forward angles to over 2.0 at backward angles. $\mathrm{CF}_f^{\perp\perp}(\psi)$, $\mathrm{CF}_f^{\parallel\parallel}(\psi)$, and $\mathrm{CF}_f^{\perp\parallel}(\psi)$ exhibit a unique feature of minimum in the region of $\psi = 85° - 100°$. In this region theoretical simulations show very small values of $\hat{\beta}_p^{\perp\perp}(\psi)$, $\hat{\beta}_p^{\parallel\parallel}(\psi)$, and $\hat{\beta}_p^{\perp\parallel}(\psi)$, which is illustrated for the case of 200 nm polystyrene beads in Figs. 1(b)–1(d). When only parallel light is detected, the values near 90° are predicted to be nearly zero, with the minimum value at 90° for $\hat{\beta}_p^{\parallel\parallel}(\psi)$ and at 95° for $\hat{\beta}_p^{\perp\parallel}(\psi)$. This is to be expected for light scattered by small particles. The Mie calculations show that the combination of perpendicularly polarized incident and detected light also produces very small values of $\hat{\beta}_p^{\perp\perp}(\psi)$ over the angular range 85°–100° [Fig. 1(c)]. Resolving the small values of $\beta_p^{\perp\perp}(\psi)$, $\beta_p^{\parallel\parallel}(\psi)$, and $\beta_p^{\perp\parallel}(\psi)$ over the angular range 85°–100° with the LISST-VSF is challenging due to low detected signal relative to background signal. Furthermore, uncertainty in the reference values of $\hat{\beta}_p^{\perp\perp}(\psi)$, $\hat{\beta}_p^{\parallel\parallel}(\psi)$, and $\hat{\beta}_p^{\perp\parallel}(\psi)$ can be expected due to sensitivity of the Mie scattering calculations to input parameters characterizing the bead suspensions. As a result, values of $\mathrm{CF}_f^{\perp\perp}(\psi)$, $\mathrm{CF}_f^{\parallel\parallel}(\psi)$, and $\mathrm{CF}_f^{\perp\parallel}(\psi)$ within the range $\psi = 85° - 100°$ were set to their respective value at 85° (Fig. 2).

The final data products of $\beta_p(\psi)$, $\mathrm{DoLP}_p(\psi)$, and $p_{22}(\psi)$ obtained with corrected $\beta_p^{\parallel\perp}(\psi)$, $\beta_p^{\perp\perp}(\psi)$, $\beta_p^{\parallel\parallel}(\psi)$, and $\beta_p^{\perp\parallel}(\psi)$ were determined for six polystyrene bead suspensions with diameters between 100 nm and 2 µm and compared with earlier results obtained in Ref. [25] from Mie scattering calculations and corrected LISST-VSF measurements. We present example results for 200 nm and 2 µm beads in Fig. 3 while recalling that 2 µm beads were not used in the determination of calibration correction functions. For $\beta_p(\psi)$ and $\mathrm{DoLP}_p(\psi)$, the results are nearly indistinguishable between earlier $\mathrm{CF}_f(\psi)$-corrected LISST-VSF measurements and new $\mathrm{CF}_f^{\epsilon\epsilon}(\psi)$-corrected LISST-VSF measurements, and they both

agree very well with reference values obtained with Mie scattering calculations [Figs. 3(a) – 3(d)]. Although such comparisons for larger beads in Figs. 3(b) and 3(d) can be affected by the presence of sharp interference maxima and minima, we found that if these oscillations are disregarded the corrected measurements and theoretical calculations of $\beta_p(\psi)$ and $\mathrm{DoLP}_p(\psi)$ for larger beads are generally in good agreement [25].

An advantage of the $\mathrm{CF}_f^{\epsilon\epsilon}(\psi)$ correction scheme is that it allows for improved estimations of $p_{22}(\psi)$ from LISST-VSF measurements [Figs. 3(e) and 3(f)]. Recall that Koestner *et al.* [25] did not examine $p_{22}(\psi)$ and hence did not establish any corrections for $p_{22}(\psi)$. The results presented in Figs. 3(e) and 3(f) labeled uncorrected are from standard manufacturer's processing. Note also that for a collection of optically inactive homogenous spheres, which is an approximate assumption for polystyrene beads, $p_{22}(\psi)$ is expected to be 1 for all angles [1,26,38]. Results for $\psi = 35°–55°$ and $125°–145°$ are not shown in Fig. 3(e) and 3(f) because our measurements do not have dependence on $p_{22}(\psi)$ at $\psi = 45°$ and 135° [Eq. (3)]. Outside these two angular ranges, the estimates of $p_{22}(\psi)$ after $\mathrm{CF}_f^{\epsilon\epsilon}(\psi)$ correction show significant improvement compared to standard manufacturer's results, particularly for $\psi > 55°$. For

example, in the angular range $\psi = 70° - 110°$ the corrected values of $p_{22}(\psi)$ are quite close to a reference value of 1 for 200 nm beads, and the root mean square deviation (RMSD) calculated using the reference value of 1 decreases almost an order of magnitude compared to uncorrected results obtained with standard manufacturer's processing. The dotted lines representing 25th and 75th percentile data suggest that $p_{22}(\psi)$ is more subject to variations between replicate measurements than $DoLP_p(\psi)$ because this interquartile range is on average 30%–40% larger for $p_{22}(\psi)$ than for $DoLP_p(\psi)$. From these results, two angles are chosen to provide the most reliable data of $p_{22}(\psi)$ from the LISST-VSF measurements following our correction: $\psi = 20°$ and $100°$.

The estimates of RMSD between $CF_f^{\epsilon\epsilon}(\psi)$-corrected measured and reference values for 2 μm beads are 15%, 0.13, and 3% for $\beta_p(\psi)$, $DoLP_p(\psi)$, and $p_{22}(\psi)$, respectively. The percent RMSD indicates the normalization of deviations to reference values; for $DoLP_p(\psi)$ no normalization was applied. These RMSD estimates are based on including all scattering angles with the exception that $p_{22}(\psi)$ only includes the angular ranges of 16°–25° and 70°–110°. We expect actual uncertainty in $\beta_p(\psi)$, $DoLP_p(\psi)$, and $p_{22}(\psi)$ to be much lower than the above estimates of RMSD because the reference values for larger beads within the interference maxima and minima are expected to be particularly sensitive to uncertainties in input data to Mie scattering calculations. If we consider 200 nm beads as having more accurate reference values owing to a smooth angular scattering pattern, the RMSDs for $\beta_p(\psi)$, $DoLP_p(\psi)$, and $p_{22}(\psi)$ are only 1%, 0.004, and 0.41%, respectively. Furthermore, the RMSD for $p_{22}(\psi)$ at the angles of most interest to the current study (20° and 100°) is less than 1% as determined by comparing our corrected results with a reference value of 1 for all bead sizes evaluated.

B. Polarized Light Scattering and Particle-Size Fractionation

In this section, we evaluate changes in the polarized light scattering metrics, $DoLP_p(\psi)$ and $p_{22}(\psi)$, following particle-size fractionation of seawater samples that are characterized by contrasting natural particle assemblages. All measurements of $DoLP_p(\psi)$ and $p_{22}(\psi)$ collected on original (unfractionated) seawater samples and size-fractionated samples obtained following fractionation with 5 μm and 20 μm mesh are presented in Fig. 4. All optical parameters for each sample represent median values based on 200–400 replicate measurements for a given sample unless specified otherwise. These seawater samples have been thoroughly characterized to represent contrasting natural assemblages of particles from coastal environments, including near-shore samples dominated by organic particulate matter with the predominant role of small-sized or large-sized phytoplankton cells, estuarine samples dominated by inorganic particles, and offshore samples representative of phytoplankton-dominated subsurface chlorophyll-a maximum and near-surface water dominated by organic non-algal particles [25,27]. To further illustrate the variability within our samples, we present values of several parameters used in characterizing the particulate assemblages in Table 3.

Table 3.   Range of Particulate Characteristics and Number of Samples

Particle Parameter	Min	Max	N
c_p [m^{-1}]^a	0.41	21	46
SPM [g m^{-3}]	0.24	74	27
POC [g m^{-3}]	0.063	2.9	27
Chla [mg m^{-3}]	0.53	6.0	15
POC/SPM	0.039	0.64	27
D_v^{50} [μm]	4.5	25	41
D_v^{90} [μm]	8.1	37	41

^{a}Particulate attenuation coefficient from LISST-VSF, $\lambda = 532$ nm.

In general, the angular shapes of $DoLP_p(\psi)$ are similar with an upside-down U-shaped curve with maximum values $DoLP_{p,max}$ near $\psi = 90°$, and these results are consistent with previously reported measurements of natural assemblages of marine particles [19–21]. Importantly, however, there is some noticeable variability in data obtained with our samples [Figs. 4(a)–4(c)]. Although the range of $DoLP_p(\psi)$ values appears similar for the unfractionated [Fig. 4(c)] and size-fractionated [Figs. 4(a) and 4(b)] samples, the median values are higher for the size-fractionated samples compared to the unfractionated samples in the angular region associated with $DoLP_{p,max}$.

At scattering angles $\psi < 25°$ and $\psi = 70° - 110°$ features associated with unstable solutions of $p_{22}(\psi)$ are minimized or avoided. At these angles the measurements with polystyrene bead suspensions also showed reduced uncertainties as seen in the dotted lines representing the 25th and 75th percentile data in Fig. 3. Therefore, these angular ranges are best suited for the analysis of $p_{22}(\psi)$ obtained from measurements of the LISST-VSF [Figs. 4(d)–4(f)]. Our determinations of $p_{22}(\psi)$ for seawater samples show values typically larger than 0.90 for nearly all scattering angles reported, and the shape is relatively flat for $\psi > 70°$ [Figs. 4(d)–4(f)]. For $\psi < 25°$, $p_{22}(\psi)$ is generally larger than it is for $\psi > 70°$. The values of $p_{22}(\psi)$ from our measurements are slightly higher or about the same as the literature values for seawater samples [19–21]. The values of $p_{22}(\psi)$ close to 1 could suggest random orientation of nonspherical particles and/or the presence of nonspherical particles with aspect ratios close to 1 [43,44]. Our measurements were made on natural assemblages of aquatic particles that exhibit great heterogeneity in terms of size, shape, inter- and intra-particle composition, and internal structures. Most likely, however, particles were in random orientation during our measurements, which appears to indicate that such highly complex assemblages of particles in random orientation behave, in terms of $p_{22}(\psi)$, similarly to spherical particles and/or nonspherical particles with aspect ratios close to 1. As mentioned previously, the specific angles at which $p_{22}(\psi)$ is evaluated for the remainder of the current study are 20° and 100°.

Box plots of metrics derived from the measurements of $DoLP_p(\psi)$ and $p_{22}(\psi)$ are shown in Fig. 5. For all measurements, $DoLP_{p,max}$ ranges from approximately 0.65 to 0.90, with the lowest value associated with one of the unfractionated samples and the highest value associated with one of the 5 μm filtrates [Fig. 5(a)]. The angles associated with $DoLP_{p,max}$,
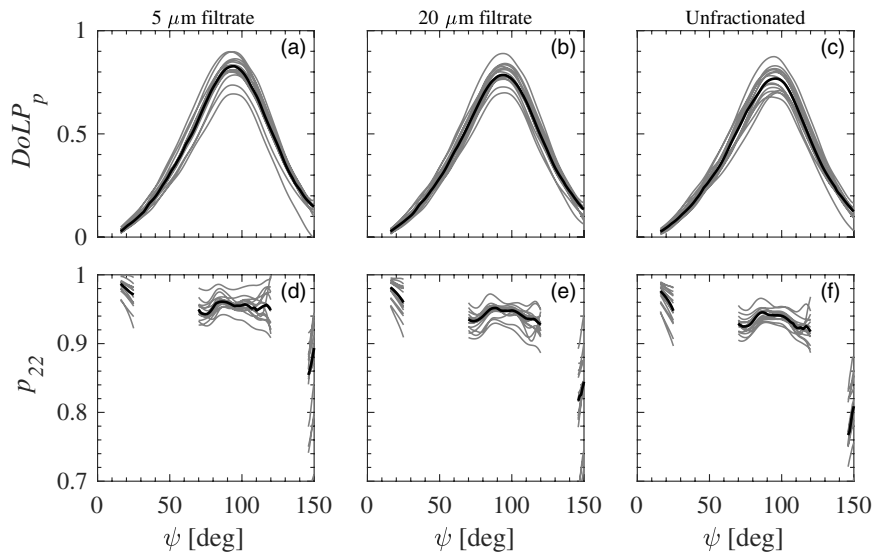
Fig. 4. Measured (a)–(c) $\mathrm{DoLP}_p(\psi)$ and (d)–(f) $p_{22}(\psi)$ for unfractionated and size-fractionated samples of all seawater samples as indicated above each column. Data for $p_{22}(\psi)$ are not shown for $\psi = 26° - 69°$ and $\psi = 121° - 145°$. Solid black lines are median values of $\mathrm{DoLP}_p(\psi)$ and $p_{22}(\psi)$ determined from all samples.
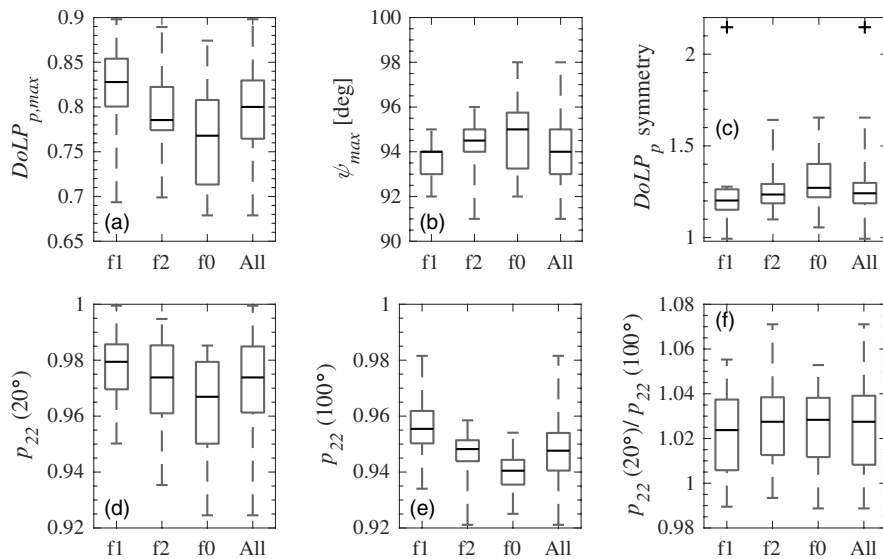

Fig. 5. Nonparametric box plots of polarized light scattering metrics derived from (a)–(c) $\mathrm{DoLP}_p(\psi)$ and (d)–(f) $p_{22}(\psi)$ data displayed in Fig. 4. The horizontal marks of each box plot in order from bottom to top represent the minimum, first quartile, median, third quartile, and maximum values from each data set excluding outliers. Three box plots are shown in each panel as indicated with f1 for 5 μm filtrate, f2 for 20 μm filtrate, and f0 for unfractionated seawater. A fourth box plot is shown using all unfractionated and size-fractionated samples. Outliers are marked with a cross in (c) for being greater than 4 times the interquartile range from the third quartile.

i.e., $\psi_{\max}$, are within the range 91°–98°, and the median values of $\psi_{\max}$ derived from the unfractionated samples, 20 μm filtrates, and 5 μm filtrates are all within a small angular range of 94°–95° [Fig. 5(b)]. The range of $p_{22}(20°)$ is larger relative to $p_{22}(100°)$ such that interquartile range of $p_{22}(20°)$ is 2–3 times larger than the interquartile range of $p_{22}(100°)$. A noteworthy trend seen in Figs. 5(a) and 5(e) is an increase in the 25th, 50th, and 75th percentile values of $\mathrm{DoLP}_{p,\max}$ and $p_{22}(100°)$ with decreasing proportion of large-sized particles in the samples (i.e., from unfractionated samples to 20 μm filtrates to 5 μm filtrates). Changes in terms of magnitude of $\mathrm{DoLP}_p(\psi)$ are

more substantial than $p_{22}(100°)$. A similar, but weaker, trend is seen for $p_{22}(20°)$; however, it only exists for the 50th and 75th percentile data [Fig. 5(d)].

Parameters that characterize the angular shape of $\mathrm{DoLP}_p(\psi)$ and $p_{22}(\psi)$ are presented in Figs. 5(c) and 5(f). Although the angular pattern of $\mathrm{DoLP}_p(\psi)$ is not perfectly symmetrical, it is significantly more symmetrical than the strongly forward peaked $\beta_p(\psi)$ of marine particles. The DoLP_p symmetry parameter indicates that $\mathrm{DoLP}_p(\psi)$ for the examined seawater samples is more skewed towards forward angles because values of this parameter are larger than 1 [Fig. 5(c)]. There is a general

trend of decreasing DoLP_p symmetry factor following particle-size fractionation with 20 μm and then 5 μm mesh; the median values are highest for unfractionated samples and lowest for 5 μm filtrates [Fig. 5(c)]. The lowest value of DoLP_p symmetry factor close to 1 was observed for one of the 5 μm filtrates and represents the highest symmetry among the samples.

The ratio of $p_{22}(20°)/p_{22}(100°)$ is used to characterize the change of $p_{22}(\psi)$ between these two scattering angles. We see that $p_{22}(20°)$ is greater than $p_{22}(100°)$ for nearly all seawater samples, albeit by at most 7% [Fig. 5(f)]. There appears to be no trend associated with changes in $p_{22}(20°)/p_{22}(100°)$ following particle-size fractionation.

A one-way analysis of variance was performed for the data presented in Fig. 5 to test the statistical significance of the trends observed following particle-size fractionation. These tests established that the only metrics with statistically significant differences as a result of fractionation are $p_{22}(100°)$ and $\mathrm{DoLP}_{p,\max}$ (the level of marginal significance $p = 0.0002$ and $p = 0.025$, respectively).

C. Relationships Between $\mathrm{DoLP}_p(\psi)$, $p_{22}(\psi)$, and Particle Characteristics

In this section relationships between polarized light scattering metrics derived from the 46 measurements of $\mathrm{DoLP}_p(\psi)$ and $p_{22}(\psi)$ and corresponding particle composition or size parameters are evaluated. Each sample that has measurements with LISST-VSF and measurements of PSD or particulate composition is treated as an independent sample, i.e., size-fractionated samples are treated as independent of their original (unfractionated) sample to increase the size of data set used in the analysis of relationships. This is reasonable, as changes in both composition and size distribution are observed after particle-size fractionation [27], and changes in $\mathrm{DoLP}_p(\psi)$ and $p_{22}(\psi)$ after fractionation are comparable to changes between different unfractionated samples (Figs. 4 and 5). We note that the fractionation efficiency for these natural assemblages of marine particles was non-ideal, and information describing the quality of particle-size fractionation is provided in our other publication [27]. This limitation is not relevant with regards to the present study.

In Fig. 6 correlations of polarized light scattering metrics, and corresponding particle composition or size parameters are evaluated using Pearson and Spearman correlation coefficients, R and ρ, respectively. The ratios POC/SPM, Chla/SPM, and $a_{ph}(440)/a_p(440)$ are used to quantify composition of particulate matter. Note that the particulate backscattering ratio $\tilde{b}_{bp}$ is also included as a particle parameter. This parameter has been reported as a potential proxy for particle composition [45–47], although it must be recognized that $\tilde{b}_{bp}$ is also dependent on particle size [45,48]. Characterization of PSDs using the percentile particle diameters D_v^{50} and D_v^{90} reflects the contribution of small- versus large-sized particles such that higher values indicate increased contributions of large-sized particles to the particulate assemblage.

Figure 6(a) presents Pearson correlation coefficients R, determined from untransformed variables under the assumption that linear relationships provide proper representation of the data. This is a reasonable assumption following visual inspection of

the 42 variable pairs evaluated. Nonetheless, in Fig. 6(b) we also present Spearman rank correlation coefficients ρ, which assess the strength of monotonic association between variables, which generally can be linear or nonlinear. In general, the two different means of evaluating correlation show similarities in terms of which pairs of variables produce weak, moderate, and strong correlation (Fig. 6).

This correlation analysis provides further evidence to some of the trends discussed in Section 3.B. For the relationships between parameters associated with $\mathrm{DoLP}_p(\psi)$ and the particulate characteristics, the strongest correlation exists for $\mathrm{DoLP}_{p,\max}$ and D_v^{90}. There is only moderate correlation for $\mathrm{DoLP}_{p,\max}$ and D_v^{50}. The observation that a stronger correlation is found between $\mathrm{DoLP}_{p,\max}$ and D_v^{90} than that obtained between $\mathrm{DoLP}_{p,\max}$ and D_v^{50} is likely due to the depolarizing influence of large-sized particles on light. The light depolarization increases when the relative abundance of large-sized particles increases, and the relative abundance of large-sized particles is better captured by D_v^{90} compared to D_v^{50}. Additionally, $\mathrm{DoLP}_{p,\max}$ has weak correlation with particle composition parameters. Previous measurements with individual populations of phytoplankton cells and silt particles suggested that $\mathrm{DoLP}_{p,\max}$ could distinguish between phytoplankton and mineral particles with lower values indicating mineral-dominated assemblages [14,16]. However, observations of various phytoplankton species have also indicated decreases in $\mathrm{DoLP}_{p,\max}$ that can be related to morphological features associated with inner structures and cell wall surfaces [15]. The analysis of our data set suggests that measurements of $\mathrm{DoLP}_{p,\max}$ for natural assemblages of marine particles are unlikely to distinguish between organic- and inorganic-dominated assemblages or phytoplankton- and non-phytoplankton-dominated assemblages, at least in terms of the bulk compositional parameters that are included in our study (Fig. 6). Other parameters, such as $\psi_{\max}$, FWHM, and DoLP_p symmetry factor, which are associated with the angular pattern of the $\mathrm{DoLP}_p(\psi)$ function, show either weak or moderate correlation with particle parameters (Fig. 6).

When interpreting the data of $\mathrm{DoLP}_p(\psi)$ it is also important to recognize that multiple scattering is likely to result in lower values of $\mathrm{DoLP}_{p,\max}$ [49]. In our experiments appropriate measures were taken to ensure LISST-VSF measurements were made in single scattering regime [25]. To verify that multiple scattering had no significant influence on the $\mathrm{DoLP}_{p,\max}$ results, correlation coefficients of $\mathrm{DoLP}_{p,\max}$ with SPM, the particulate attenuation coefficient, and particulate scattering coefficient as indicators of total particle concentration in the samples were computed (not shown). No significant correlation was observed ($R \approx -0.16$; $\rho \approx -0.28$), suggesting that multiple scattering played insignificant role within the range of particle concentration in the examined samples.

Figure 6 also shows that the scattering matrix element $p_{22}(\psi)$ has potential to serve as an optical proxy for particle composition. Specifically, $p_{22}(20°)$ and $p_{22}(20°)/p_{22}(100°)$ show consistently strong correlation with all particle composition parameters. For example, the values of correlation coefficients R and ρ between Chla/SPM and $p_{22}(20°)$ or $p_{22}(20°)/p_{22}(100°)$ are all in the range 0.78–0.82. This result suggests that $p_{22}(20°)$ or $p_{22}(20°)/p_{22}(100°)$ can provide

(a)

	$\tilde{b}_{bp}$	POC/SPM	Chla/SPM	$a_{ph}(440)/a_p(440)$	D_v^{50}	D_v^{90}
$DoLP_{p,max}$	-0.17	0.25	0.12	0.18	-0.42	**-0.60**
ψ_{max}	-0.44	0.27	0.38	0.44	0.23	0.20
FWHM	0.22	0.02	-0.37	-0.39	-0.08	-0.25
$DoLP_p$ symmetry	0.54	-0.31	-0.30	-0.28	0.16	0.35
$p_{22}(20°)$	**-0.67**	**0.73**	**0.79**	**0.66**	0.12	-0.17
$p_{22}(100°)$	0.20	0.05	0.03	-0.11	-0.38	**-0.62**
$p_{22}(20°)/p_{22}(100°)$	**-0.76**	**0.68**	**0.78**	**0.71**	0.33	0.20
N	46	27	15	15	41	41

(b)

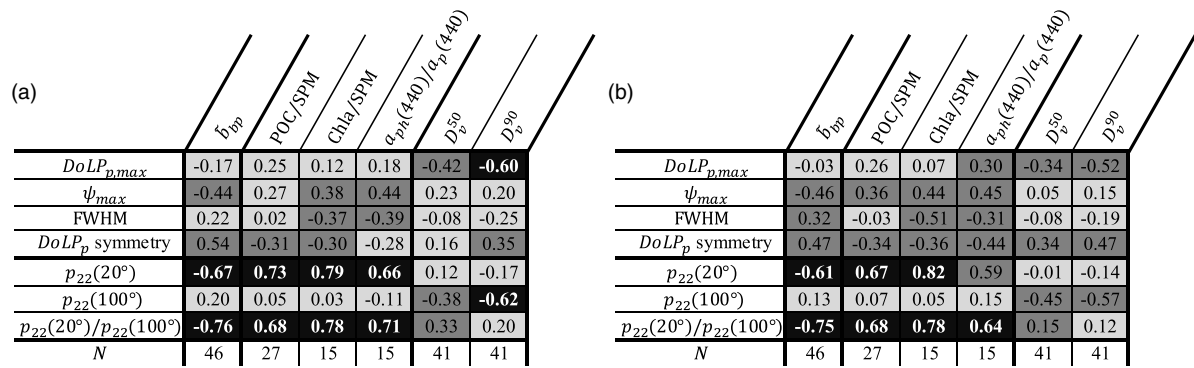|	$\tilde{b}_{bp}$	POC/SPM	Chla/SPM	$a_{ph}(440)/a_p(440)$	D_v^{50}	D_v^{90}
$DoLP_{p,max}$	-0.03	0.26	0.07	0.30	-0.34	-0.52
ψ_{max}	-0.46	0.36	0.44	0.45	0.05	0.15
FWHM	0.32	-0.03	-0.51	-0.31	-0.08	-0.19
$DoLP_p$ symmetry	0.47	-0.34	-0.36	-0.44	0.34	0.47
$p_{22}(20°)$	**-0.61**	**0.67**	**0.82**	0.59	-0.01	-0.14
$p_{22}(100°)$	0.13	0.07	0.05	0.15	-0.45	-0.57
$p_{22}(20°)/p_{22}(100°)$	**-0.75**	**0.68**	**0.78**	**0.64**	0.15	0.12
N	46	27	15	15	41	41

Fig. 6. Grids of (a) Pearson correlation coefficient R and (b) Spearman rank correlation coefficient ρ between optical parameters and particle composition or size parameters. Grids are shaded with light grey indicating weak correlation ($|R| < 0.30$), dark grey indicating moderate correlation ($0.30 \leq |R| < 0.60$), and black indicating strong correlation ($|R| \geq 0.60$). The same applies to ρ. The number of samples N containing measurements of the particle composition or size parameter taken in conjunction with scattering measurements is displayed.

useful information about the contribution of phytoplankton to the entire particulate assemblage or, more specifically, the contribution of phytoplankton versus non-algal particles to total mass concentration of particles. Importantly, while $p_{22}(20°)$ shows strong correlation with particle composition parameters, it has very weak or no correlation with particle size parameters. In contrast to $p_{22}(20°)$, the correlation coefficients between $p_{22}(100°)$ and composition parameters are very low. However, the correlation coefficients between $p_{22}(100°)$ and size parameter D_v^{90} are relatively high at the border of moderate and strong correlation, which is similar to the strength of correlation between $DoLP_{p,max}$ and D_v^{90}. It should also be pointed out that the relatively high correlation coefficients characterizing several specific cases of our analysis presented in Fig. 6 were obtained despite a relatively small range of $p_{22}(\psi)$ values [see Figs. 5(d) and 5(e)]. In addition, although the current study is primarily focused on polarized light scattering, it is worth noting that we found a very strong negative correlation ($R = -0.90$) between $\tilde{b}_{bp}$ and $a_{ph}(440)/a_p(440)$ and weak correlation of $\tilde{b}_{bp}$ with particle size parameters (not shown).

The polarized light scattering metrics, $p_{22}(20°)$ and $p_{22}(20°)/p_{22}(100°)$, that produced the strongest correlation with particle composition parameters are plotted in Fig. 7 along with linear regressions fitted to the data. For most cases illustrated in Fig. 7 there is a clear linear trend between the two variables under consideration, although data points exhibit significant scatter. A few cases [Figs. 7(a), 7(g), and 7(h)] appear to exhibit some features of a nonlinear pattern, so we also tested the exponential fit to the data by computing the linear regression for the log-transformed y variable (ordinate) versus the untransformed x variable (abscissa). The Pearson correlation coefficient R between such variables was not, however, higher compared to R values for ordinary (untransformed) variables.

The data points in Fig. 7 are shaded based on values of particle size parameter D_v^{90}. Note , for example, that data points for $D_v^{90} > 30$ μm representing the highest proportion of large-sized particles in the samples are spread throughout low and high values of both $p_{22}(20°)$ and $p_{22}(20°)/p_{22}(100°)$ along their trend lines associated with variation in particle composition parameters. Similar observation applies to data points representing D_v^{90} between 15 μm and 30 μm. This result indicates

the insensitivity of the observed relationships between both $p_{22}(20°)$ and $p_{22}(20°)/p_{22}(100°)$ and particle composition parameters to varying proportion of large-sized versus smaller particles. These polarized light scattering metrics also exhibit positive correlation with particle composition metrics of POC/SPM, Chla/SPM, and $a_{ph}(440)/a_p(440)$ in that high values of $p_{22}(20°)$ or $p_{22}(20°)/p_{22}(100°)$ relate to particulate assemblages that are generally organic or phytoplankton dominated, and low values relate to particulate assemblages that are generally inorganic or non-phytoplankton dominated. The correlation between the composition parameters and $\tilde{b}_{bp}$ is negative [Figs. 7(g) and 7(h)], which is generally consistent with the notion that higher values of $\tilde{b}_{bp}$ are expected for particle assemblages with higher contribution of inorganic or non-algal particles [45–47]. Acknowledging the complexity of natural assemblages of marine particles, significant correlations and trends presented in Fig. 7 are remarkable in that they hold up over the relatively broad range of mostly coastal waters with a few offshore locations examined in this study (Table 3).

The polarized light scattering metrics $DoLP_{p,max}$ and $p_{22}(100°)$ that produced the strongest correlation with particle size parameter, specifically D_v^{90}, are plotted in Fig. 8 along with linear regressions fitted to the data. The data points are shaded based on values of $\tilde{b}_{bp}$. Note that data points corresponding to different values of $\tilde{b}_{bp}$ are spread throughout low and high values of both $DoLP_{p,max}$ and $p_{22}(100°)$ along their trend lines associated with variation in D_v^{90}. This result indicates the insensitivity of the relationships between both $DoLP_{p,max}$ and $p_{22}(100°)$ and particle size parameter D_v^{90} to particulate assemblages with varying $\tilde{b}_{bp}$ within our data set. Because these polarized light scattering metrics show negative correlation with D_v^{90}, low values of $DoLP_{p,max}$ and $p_{22}(100°)$ relate to particulate assemblages that contain higher proportions of large-sized particles. Note also that the correlation of D_v^{90} with $p_{22}(100°)$ is somewhat improved compared to correlation with $DoLP_{p,max}$ (Fig. 8). As indicated earlier in relation to Fig. 6, the correlation between these scattering parameters and D_v^{50} are only moderate, and this is related largely to three samples that had significantly higher D_v^{50} (≈ 25 μm) than all other samples (<14 μm). These three samples were collected at the SIO Pier
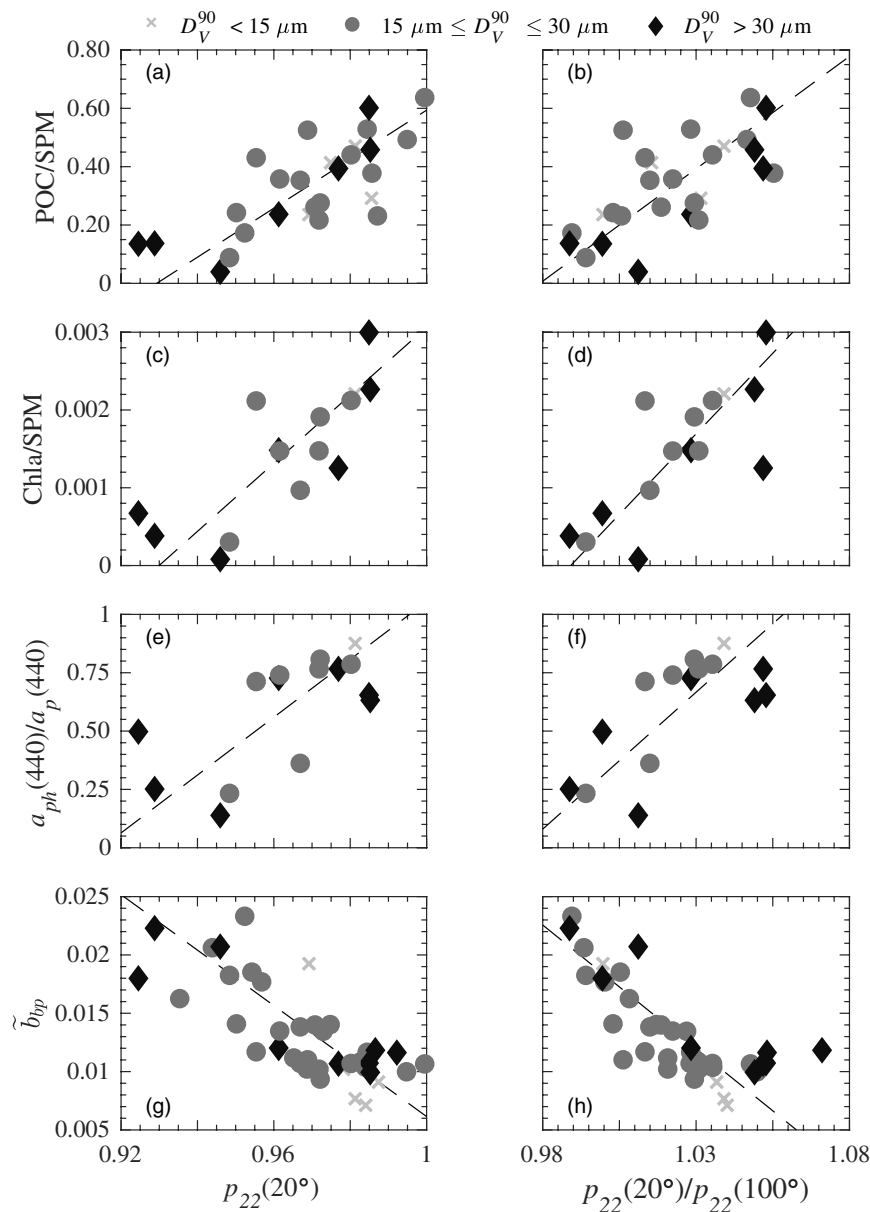
Fig. 7.   Particle compositional parameters (displayed on the *y* axis) as a function of polarized light scattering metrics (a), (c), (e), (g) $p_{22}(20°)$ and (b), (d), (f), (i) $p_{22}(20°)/p_{22}(100°)$ from measurements with seawater samples. Data points are shaded by the value of D_v^{90} as indicated in legend. Linear regressions are plotted with a black dashed line.

coinciding with observations of increased presence of large chain-forming diatoms using Scripps Plankton Camera System (spc.ucsd.edu). These three samples are no longer outliers in the relationships between D_v^{90} and $\text{DoLP}_{p,\text{max}}$ or $p_{22}(100°)$ presented in Fig. 8. Although the data points in Fig. 8 exhibit significant scatter with the correlation coefficient R of about 0.6, it is noteworthy that these trends hold up over the broad range of complex natural assemblages of marine particles examined in this study. These findings are also generally consistent with previous measurements of Voss and Fry [21], who observed the largest variability in $\text{DoLP}_p(\psi)$ and $p_{22}(\psi)$ between seawater samples for scattering angles 90° and 100°, respectively. Although Voss and Fry [21] did not characterize the suspended particles, it can be speculated that the particle assemblages they

examined were mostly organic dominated and varied more considerably in terms of PSD than composition because measurements were made in mainly offshore Atlantic and Pacific waters.

Deviations of $p_{22}(\psi)$ from 1 can be generally considered to be associated with particle nonsphericity, as $p_{22}(\psi)$ is equal to 1 at all scattering angles for homogenous and optically inactive spheres [1,26,38]. When samples contain irregularly shaped particles such as those found in seawater, the behavior of $p_{22}(\psi)$ is also confounded by the effects of complex refractive index, size, shape, and orientation [43,44]. Measurements of $p_{22}(\psi)$ for aerosol particles indicated, for example, that minima of $p_{22}(\psi)$ are seen within the side-scattering angular range, and
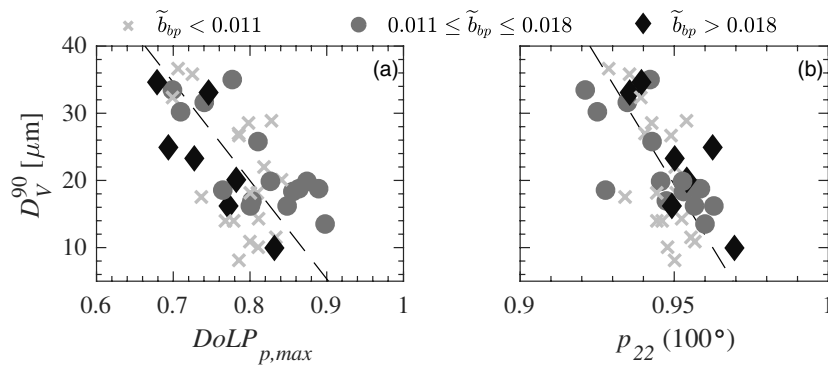
Fig. 8. Particle size parameter D_v^{90} as a function of polarized light scattering metrics (a) $DoLP_{p,\max}$ and (b) $p_{22}(100°)$ obtained from measurements with seawater samples. Data points are shaded by the value of $\tilde{b}_{bp}$ as indicated in legend. Linear regressions are plotted with a black dashed line.

lower magnitudes of minima are associated with samples containing larger-sized particles [17]. This generally concurs with our findings in that $p_{22}(100°)$ correlates negatively with D_v^{90}.

The average $p_{22}(20°)$ for mineral-dominated aerosol particles reported by Volten et al. [6] is relatively low, 0.89. This suggests that such deviations from $p_{22}(20°) = 1$ could be in response to the presence of particles with higher refractive index. The seawater sample from the current study with the lowest $p_{22}(20°)$ has a value of about 0.92. This sample (referred to as P_R in Ref. [27]) was collected at the SIO Pier after a significant rain event and has a relatively low value of POC/SPM = 0.14, which is similar to our samples from San Diego River Estuary. Given this POC/SPM value, it is reasonable to assume sample P_R had a significant proportion of mineral particles, which is consistent with the data of Volten et al. [6] for mineral-dominated aerosols. Additionally, there is one seawater sample in our study with a value of $p_{22}(20°)$ that is nearly 1, so it deviates most significantly from lower values that are presumably characteristic of mineral-dominated assemblages. In this case, it is the 5 μm filtrate of seawater collected at the SIO Pier location during high abundance of phytoplankton. This filtrate sample has the highest POC/SPM (= 0.64) of all samples examined in this study, indicating virtually an entirely organic assemblage. The results for these example mineral-dominated and organic-dominated samples are naturally consistent with the general trend presented in Fig. 7(a).

The correlation of $p_{22}(20°)$ with particle composition parameters such as POC/SPM, and not particle size parameters, is of significance because the increases in $p_{22}(20°)$ following particle-size fractionation [Fig. 5(d)] are therefore more likely to be related to changes in bulk particle composition than PSD. This suggests that, for our samples, small- and medium-sized particles may be more organic dominated than larger particles that are removed by the 5 μm and 20 μm mesh filters. This is further corroborated with more direct compositional measurements, i.e., POC/SPM of the 5 μm filtrate was higher than the unfractionated sample for 9 out of the 12 samples that have measurements of POC and SPM on both the unfractionated and 5 μm filtered samples.

Given that $p_{22}(\psi)$ is near 1 and therefore the matrix elements $p_{22}(\psi)$ and $p_{11}(\psi)$ are similar [Eq. (12)], we additionally examined correlations of the particulate phase

function $(\tilde{\beta}_p(\psi) = \beta_p(\psi)/b_p)$ with the particle size and composition parameters. This analysis demonstrated that $\tilde{\beta}_p(20°)/\tilde{\beta}_p(100°)$ exhibited strong positive correlation with compositional parameters, which is consistent with findings for $p_{22}(20°)/p_{22}(100°)$. However, in contrast to $p_{22}(100°)$, $\tilde{\beta}_p(100°)$ exhibited weak correlation with particle size parameters ($R < 0.17$). Furthermore, in contrast to $p_{22}(20°)$, $\tilde{\beta}_p(20°)$ exhibited at most moderate negative correlation with particle composition parameters ($R = -0.15$ to -0.44). These findings suggest that $p_{22}(\psi)$ does not necessarily carry similar information to the phase function and further support the notion that $p_{22}(\psi)$ can be uniquely sensitive to particulate characteristics.

We also investigated relationships between the particle size and composition parameters shown in Fig. 6, but the results are not shown. These size and composition metrics have weak correlation ($|R|$ and $|\rho| < 0.3$), except for correlations between D_v^{50} and Chla/SPM or $a_{ph}(440)/a_p(440)$ which are moderate, $|R|$ and $|\rho| < 0.45$. This result further supports the general complexity of natural assemblages of marine particles, e.g., samples containing significant proportions of large particles can be organic or inorganic dominated.

Following observations of improved correlation of the median values of $DoLP_{p,\max}$ with the particle size parameter D_v^{90} as compared to D_v^{50} (Fig. 6), as well as a decreasing trend of median values of $DoLP_{p,\max}$ with D_v^{90} [Fig. 8(a)], here we further investigate relationships between other percentile-based values of $DoLP_{p,\max}$ (i.e., the 10th and 90th percentiles) and D_v^{90}. As mentioned earlier, we averaged 200–400 replicate measurements to obtain representative median values of scattering parameters for a given seawater sample. In our further analysis of $DoLP_p(\psi)$, we take advantage of variations between replicate measurements for a given seawater sample to calculate different percentiles, such as the 10th percentile data that can represent the rare low values and the 90th percentile data can represent the rare high values of $DoLP_p(\psi)$, each isolating the influence of different particle sizes/types in suspension. This additional analysis is driven by the expectation that lower-percentile values of $DoLP_{p,\max}$ are more strongly associated with the relatively rare and larger-sized particles influencing D_v^{90} compared to higher-percentile values of $DoLP_{p,\max}$.

Figures 9(a)–9(c) present D_v^{90} plotted as a function of the 10th, 50th, and 90th percentile values of $DoLP_{p,\max}$
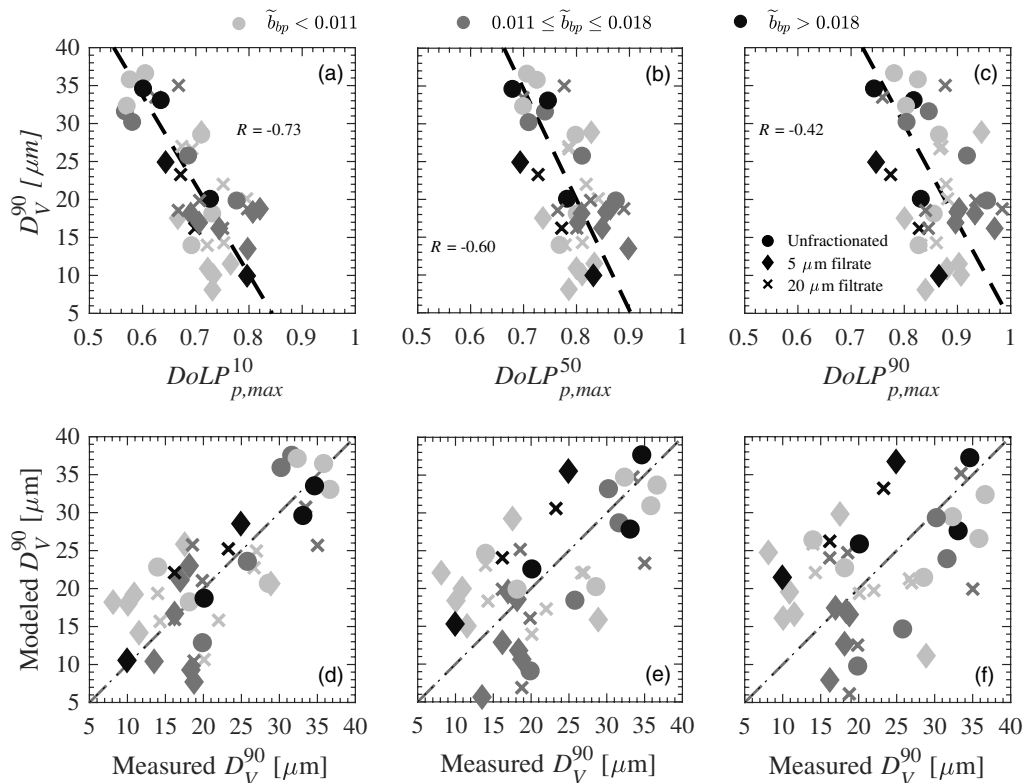
Fig. 9. Particle size parameter D_v^{90} as a function of (a) 10th percentile, (b) 50th percentile, and (c) 90th percentile $\text{DoLP}_{p,\max}$. Data points are shaded by the value of $\tilde{b}_{bp}$ as indicated in legend. The symbols of data points correspond to unfractionated and fractionated samples as indicated in panel (c). Linear regressions are plotted with black dashed lines and Pearson correlation coefficients R are displayed in each panel. Bottom panels (d)–(f) present model performance using the model-derived values from regression in the panel above [(a), (b), and (c), respectively] versus the measured D_v^{90}. A type II linear regression of modeled versus measured D_v^{90} is plotted with a gray dashed line, and a 1:1 dotted line is also plotted which is essentially indistinguishable from the regression line.

(i.e., $\text{DoLP}_{p,\max}^{10}$, $\text{DoLP}_{p,\max}^{50}$, and $\text{DoLP}_{p,\max}^{90}$, respectively) derived from the 200–400 replicate LISST-VSF measurements for each sample. Note that $\text{DoLP}_{p,\max}^{50}$ is here equivalent to the median $\text{DoLP}_{p,\max}$ used throughout this paper, and the data points shown in Fig. 9(b) are identical to those in Fig. 8(a). The lower percentile data corresponds to a shift towards lower values of $\text{DoLP}_{p,\max}$. For example, while the range of $\text{DoLP}_{p,\max}^{10}$ for all examined samples is 0.57–0.82, the corresponding range of $\text{DoLP}_{p,\max}^{90}$ is 0.75–0.99. As could be expected, the correlation between D_v^{90} and $\text{DoLP}_{p,\max}$ is significantly higher ($R = -0.73$) for $\text{DoLP}_{p,\max}^{10}$ when compared to correlations with $\text{DoLP}_{p,\max}$ derived from higher-percentile values of $\text{DoLP}_p(\psi)$ [Figs. 9(a)–9(c)]. This result suggests that $\text{DoLP}_{p,\max}$ exhibits relatively higher sensitivity to intermittent presence of relatively rare large-sized particles compared to the presence of smaller particles within the interrogated volume of the sample during a series of replicate measurements with LISST-VSF. Thus, the higher the proportion of large-sized particles (i.e., the higher the value of D_v^{90}), the lower $\text{DoLP}_{p,\max}$, and this relationship is strongest for the low percentile value of $\text{DoLP}_{p,\max}^{10}$ [Figs. 9(a) and 9(d)]. It is important to note that large particles defined here as $>20\,\mu\text{m}$ in diameter are relatively rare in seawater samples compared with smaller particles; however, they were still present in significant enough quantities to influence our scattering measurements. Based on our

PSD measurements, particle counts in size bins $>20\,\mu\text{m}$ were between 20 and 300 particles per mL for the examined samples (not presented). Acknowledging that the LISST-VSF laser beam illuminates about 1 mL per measurement scan, it is reasonable to expect that a sufficient number of large particles was encountered within the interrogated sample volume over the course of replicate measurements to influence the scattering results.

The regression fits determined in Figs. 9(a)–9(c) were used in the comparison of model-predicted D_v^{90} versus measured D_v^{90}, which is illustrated in Figs. 9(d)–9(f). Table 4 presents regression parameters for the results shown in Figs. 9(a)–9(c) as well as model-performance statistical parameters derived from the results shown in Figs. 9(d)–9(f). These statistical parameters support improved prediction of D_v^{90} from lower-percentile $\text{DoLP}_{p,\max}$ data (represented here by $\text{DoLP}_{p,\max}^{10}$) compared with higher-percentile $\text{DoLP}_{p,\max}$ data (represented here by $\text{DoLP}_{p,\max}^{50}$ and $\text{DoLP}_{p,\max}^{90}$).

The results in Fig. 9 emphasize that the relatively rare low values of $\text{DoLP}_{p,\max}$ occurring during a series of replicate measurements relate most closely to the particle size parameter, which is strongly influenced by the presence of large-sized particles. Therefore, for the examined samples it is primarily the large-sized particles that tend to decrease $\text{DoLP}_{p,\max}$ in the side angle region near 90°. Note that these trends appear to be independent of particulate composition as shown by the

Table 4. Best-Fit Regression Coefficients and Statistical Variables Evaluating Model Performance[a]

		Regression				Model Performance			
Optical Parameter	Particle Parameter	Eq.	m	b	R	RMSD	MdAPD	MdR	MB_{log}
$DoLP^{10}_{p,max}$	D_V^{90}	Linear	-117.50	104.13	-0.73	$5.83\,\mu m$	$22.9\,\%$	1.02	1.00
$DoLP^{50}_{p,max}$	D_V^{90}	Linear	-146.32	137.02	-0.60	$7.19\,\mu m$	$29.1\,\%$	1.04	0.99
$DoLP^{90}_{p,max}$	D_V^{90}	Linear	-129.06	133.14	-0.42	$8.66\,\mu m$	$36.8\,\%$	0.96	0.98
$\dfrac{\beta^{\parallel\perp}(110°)}{\beta^{\parallel\parallel}_p(110°)}$	D_V^{90}	Linear	-23.47	156.16	-0.66	$6.62\,\mu m$	$21.5\,\%$	0.98	1.00
$\dfrac{\beta^{\parallel\perp}_p(110°)}{\beta^{\parallel\parallel}_p(18°)}$	POC/SPM	Exp	-352.87	4.57	-0.88	0.10	$17.0\,\%$	0.98	1.00
$\tilde{b}_{bp}$	POC/SPM	Exp	-145.45	2.19	-0.74	0.12	$23.6\,\%$	0.96	1.00

[a]Models are the optically based relationships for estimating particle size (D_v^{90}) and composition (POC/SPM) characteristics. Optical parameters are independent variables (x), and particle parameters are dependent variables (y). Linear equations are of the form $y = mx + b$, while exponential equations are of the form $y = be^{mx}$. For the exponential (Exp) relationships, the correlation coefficient R was determined using log-transformed POC/SPM and untransformed values of the optical parameter.

spread of data points representing variability in the composition parameter $\tilde{b}_{bp}$ (Fig. 9). Furthermore, these relationships appear to be independent of particle-size fraction, as the data points representing unfractionated and size-fractionated samples do not show any clear differences in their patterns along the main trend lines.

D. Optical Polarization-Based Proxies to Estimate Particle Characteristics

An analysis was performed to identify simple optical proxies obtained from various combinations of polarized-scattering measurements for estimating particle size and composition parameters. Specifically, ratio combinations of the four polarized light scattering measurements made by the LISST-VSF, $\beta_p^{\perp\parallel}(\psi)$, $\beta_p^{\parallel\parallel}(\psi)$, $\beta_p^{\perp\perp}(\psi)$, and $\beta_p^{\parallel\perp}(\psi)$, were evaluated for a range of scattering angles to identify the most promising simple optical proxies to estimate D_v^{90} and POC/SPM. In this context, we refer to polarized-scattering parameters as simple in a sense that they utilize only one or two scattering angles.

Linear, exponential, and power function relationships of D_v^{90} versus scattering parameters were examined utilizing measurements of 41 seawater samples. The scattering parameters were composed of ratio combinations of $\beta_p^{\perp\parallel}(\psi)$, $\beta_p^{\parallel\parallel}(\psi)$, $\beta_p^{\perp\perp}(\psi)$, and $\beta_p^{\parallel\perp}(\psi)$ computed in the range of $\psi = 20° - 120°$ with a 1° interval. Consequently, there was a total of 606 scattering parameters derived from the six unique ratio combinations at 101 scattering angles. The scattering parameter that resulted in the best performance of the relationship for predicting D_v^{90} was chosen following evaluation of Pearson correlation coefficients between D_v^{90} and a given scattering parameter as well as model-performance statistics of RMSD, MdAPD, MR, and MB_{log} characterizing differences between the predicted and measured D_v^{90} (Table 2). It was found that linear as opposed to exponential or power function relationships provided the most adequate representation of the pattern of data of D_v^{90} versus scattering parameters as well as superior model-performance statistics; therefore, below we present results based only on linear regressions. We also included $DoLP_p(\psi)$ in comparative analysis with these polarization combination-based proxies.

The Pearson correlation coefficient between the polarized-scattering parameters and D_v^{90} is presented in Fig. 10(a). Note that R values presented in Fig. 10(a) are negative but displayed as the absolute values for visualization purposes. The most significant correlation ($|R| > 0.65$) is observed between $\beta_p^{\perp\perp}(\psi_1)/\beta_p^{\parallel\parallel}(\psi_1)$ and D_v^{90} in the angular region $\psi_1 \approx 95° - 110°$. There is a large angular range of moderate correlation ($0.50 < |R| \leq 0.60$) between $DoLP_p(\psi_1)$ and D_v^{90} for $\psi_1 \approx 65° - 120°$ with the maximum correlation values near $90°$. Recall that maximum values of $DoLP_p(\psi)$ are observed near $90°$ (Fig. 4); therefore, this result is in natural agreement with the strong correlation observed for $DoLP_{p,max}$ and D_v^{90} (Fig. 6).

It is important to acknowledge that the strongest correlation alone does not necessarily indicate the most useful predictive relationship. Therefore, an assessment of model performance in terms of differences between the predicted and measured values of D_v^{90} was made to aid in selecting the best-performing scattering parameter as a proxy for D_v^{90}. As an example, we present MdAPD results for the polarization combination-based relationships in Fig. 10(b). For display purposes, the MdAPD values in Fig. 10(b) are plotted inversely such that lower values of MdAPD are lighter in shade and higher in the vertical dimension. In this case, it is the $\beta_p^{\parallel\perp}(\psi_1)/\beta_p^{\perp\perp}(\psi_1)$ measurement combination for ψ_1 ranging from about 88° to 97° that produces the lowest MdAPD $\approx 15\%$. Note also that all measurement combinations have some angles that produce relationships that have MdAPD $\approx 20\%$, except for $\beta_p^{\parallel\parallel}(\psi_1)/\beta_p^{\perp\perp}(\psi_1)$ and $\beta_p^{\perp\perp}(\psi_1)/\beta_p^{\parallel\perp}(\psi_1)$. For comparison, in the angular region associated with maximum correlations of D_v^{90} with $DoLP_p(\psi_1)$, the regressions result in MdAPD $\approx 25\% - 30\%$. Upon additional analysis of model-performance statistics describing RMSD and bias, $\beta_p^{\parallel\perp}(\psi_1)/\beta_p^{\parallel\parallel}(\psi_1)$ at scattering angle $\psi_1 = 110°$ was chosen as the scattering proxy that performs best as a predictive measure for D_v^{90} (Table 4). We note that $\beta_p^{\parallel\perp}(\psi_1)/\beta_p^{\parallel\parallel}(\psi_1)$ at scattering angles close to $110°$ would have similarly good statistics. For example, the strongest correlation of -0.68 between $\beta_p^{\parallel\perp}(\psi_1)/\beta_p^{\parallel\parallel}(\psi_1)$ and D_v^{90} was actually observed at $\psi_1 = 108°$ as compared to -0.66 at $\psi_1 = 110°$.
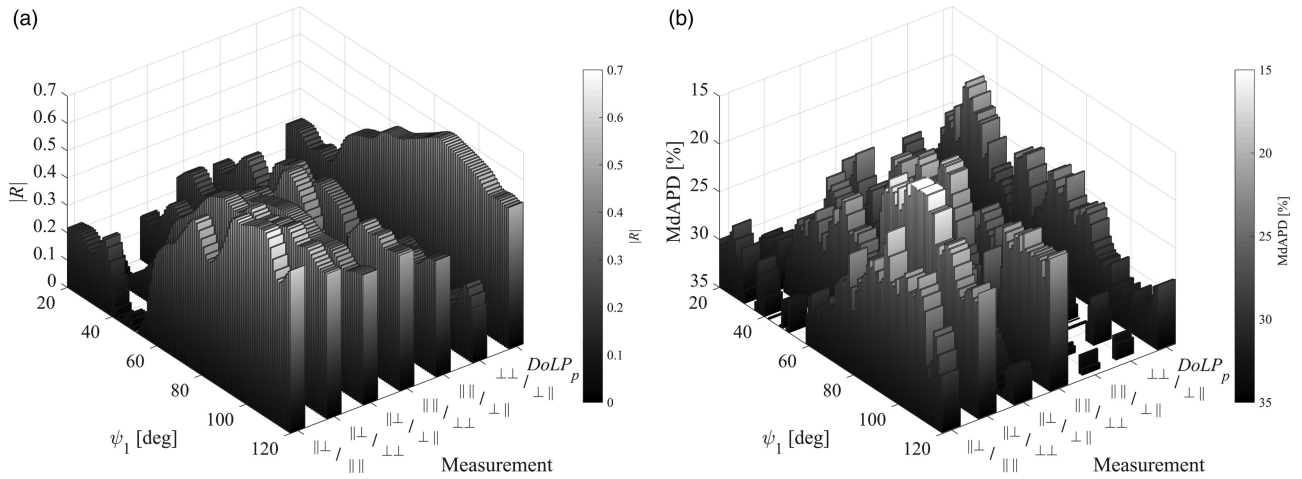
(a)

(b)

Fig. 10. (a) The absolute values of the Pearson correlation coefficient $|R|$ obtained from the analysis of 606 relationships between particle size parameter D_v^{90} and polarized light scattering parameters derived from the six unique polarization measurement combinations. Only superscript symbols of each measurement combination are shown. For example, $\| \perp / \|\|\|$ is equivalent to $\beta_p^{\|\perp}(\psi_1)/\beta_p^{\|\|\|}(\psi_1)$. See text for more detailed explanation of measurements. (b) Similar to panel (a) except that results are shown for the median absolute percent difference MdAPD determined from comparison of model-derived and measured D_v^{90}.

A similar analysis was performed for linear, exponential, and power function relationships of POC/SPM versus scattering parameters, albeit with a few noteworthy differences. First, only 27 seawater samples underwent concurrent measurements of POC, SPM, and angle-resolved polarized light scattering. Second, the six unique polarized light scattering ratios were used in this analysis with $\psi_1 = 80° - 120°$ in the numerator an $\psi_2 = 16° - 50°$ in the denominator. It was found that the exponential function provided a better fit to the data of POC/SPM versus scattering parameters as well as superior model-performance statistics compared with linear and power function fits. Therefore, below we present results only for the exponential relationships and recall that these exponential fits were determined through linear regression of log-transformed POC/SPM versus untransformed $\beta_p^{\epsilon\epsilon}(\psi_1)/\beta_p^{\epsilon\epsilon}(\psi_2)$ data.

The first important result from this analysis is that an exponential fit to the data of POC/SPM versus $\beta_p^{\|\perp}(\psi_1)/\beta_p^{\|\|\|}(\psi_2)$ performed better in terms of model-performance statistics compared to the use of other ratio combinations of polarized-scattering parameters. The values of R and MdAPD computed from relationships of POC/SPM versus $\beta_p^{\|\perp}(\psi_1)/\beta_p^{\|\|\|}(\psi_2)$ are plotted in Fig. 11(a) and Fig. 11(b), respectively. When ψ_2 ranges between about 16° and 30°, all ψ_1 angles produce $\beta_p^{\|\perp}(\psi_1)/\beta_p^{\|\|\|}(\psi_2)$ exhibiting strong correlation with POC/SPM, i.e., $|R| > 0.80$. The highest correlation coefficients of about 0.87 are observed for $\psi_1 = 95° - 120°$ [Fig. 11(a)]. The trends for MdAPD are generally similar, as R in areas of the lowest MdAPD < 20% exists in the bottom right quadrant of Fig. 11(b). The angle combination that generates the lowest MdAPD is found at $\psi_1 = 110°$ and $\psi_2 = 40°$, where MdAPD $\approx 15\%$ and $|R| = 0.81$. There is a relatively large area of strong correlation in Fig. 11(a), and when considering other statistical variables associated with model performance shown in Table 4, we chose $\beta_p^{\|\perp}(110°)/\beta_p^{\|\|\|}(18°)$ as the best polarized-scattering proxy for estimating POC/SPM. It is noteworthy that

the selected relationships to estimate POC/SPM and D_v^{90} both rely on a measurement of $\beta_p^{\|\perp}(110°)$.

Figure 12 provides a graphical summary of results associated with the selected relationships for estimating D_v^{90} from $\beta_p^{\|\perp}(110°)/\beta_p^{\|\|\|}(110°)$ and POC/SPM from $\beta_p^{\|\perp}(110°)/\beta_p^{\|\|\|}(18°)$. The corresponding information on the best-fit regression coefficients and the statistical parameters for evaluating the difference between the predicted and measured values of D_v^{90} and POC/SPM are presented in Table 4. The particle size parameter D_v^{90} as a function of $\beta_p^{\|\perp}(110°)/\beta_p^{\|\|\|}(110°)$ and the corresponding best-fit linear regression are displayed in Fig. 12(a). The values of D_v^{90} predicted from this linear regression model are plotted versus the measured D_v^{90} in Fig. 12(c). In both these graphs the data points are shaded to represent three groups associated with varying values of measured particulate backscattering ratio $\tilde{b}_{bp}$. Except for one significant outlier, the shaded data points spread rather evenly around the linear regression, which suggests that there is no clear influence of particle composition as potentially related to $\tilde{b}_{bp}$ on the examined relationship [Figs. 12(a) and 12(c)]. In terms of model performance of D_v^{90} obtained from $\beta_p^{\|\perp}(110°)/\beta_p^{\|\|\|}(110°)$ compared to the actual measured D_v^{90}, there is essentially no bias (MdR = 0.98; MB$_{log}$ = 1.00), and MdAPD is about 21% (Table 4).

The POC/SPM data as a function of $\beta_p^{\|\perp}(110°)/\beta_p^{\|\|\|}(18°)$ and the corresponding best-fit exponential relationship are displayed in Fig. 12(b), while Fig. 12(d) shows the predicted versus measured values of POC/SPM. The relationship appears insensitive to particle size as parameterized with D_v^{90}, which is indicated by the spread of shaded data points [Figs. 12(b) and 12(d)]. The modeled values of POC/SPM derived from $\beta_p^{\|\perp}(110°)/\beta_p^{\|\|\|}(18°)$ have essentially no bias when compared to measured POC/SPM, and MdAPD is 17% (Table 4). For comparison, Table 4 also shows the statistics for the relationship of POC/SPM versus $\tilde{b}_{bp}$ (not shown graphically), which was determined using the same data set of 27 seawater samples as
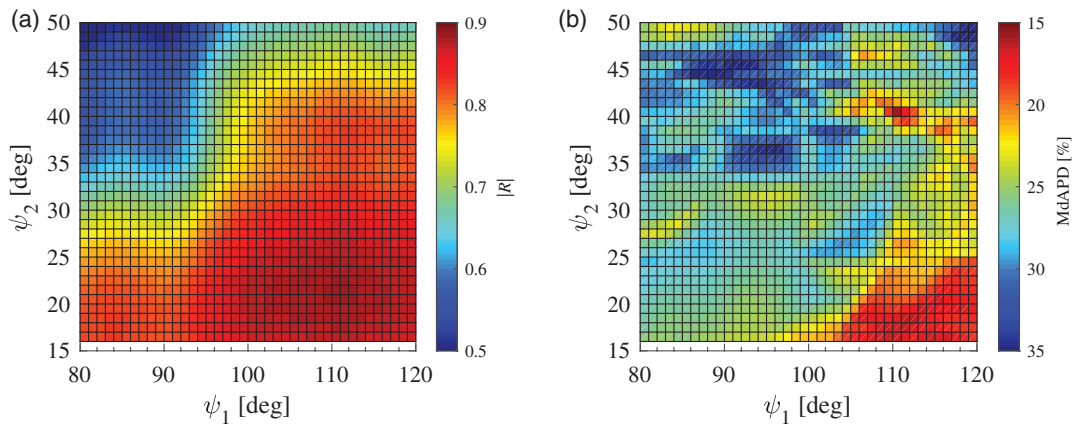
Fig. 11. Results of the analysis of 1435 relationships between particle composition parameter POC/SPM and polarized light scattering metric $\beta_p^{\parallel\perp}(\psi_1)/\beta_p^{\parallel\parallel}(\psi_2)$. Results are displayed for (a) the absolute value of the Pearson correlation coefficient $|R|$ between log-transformed POC/SPM data and ordinary (untransformed) values of the polarization parameter and (b) the median absolute percent difference MdAPD determined from comparison of model-derived and measured POC/SPM.
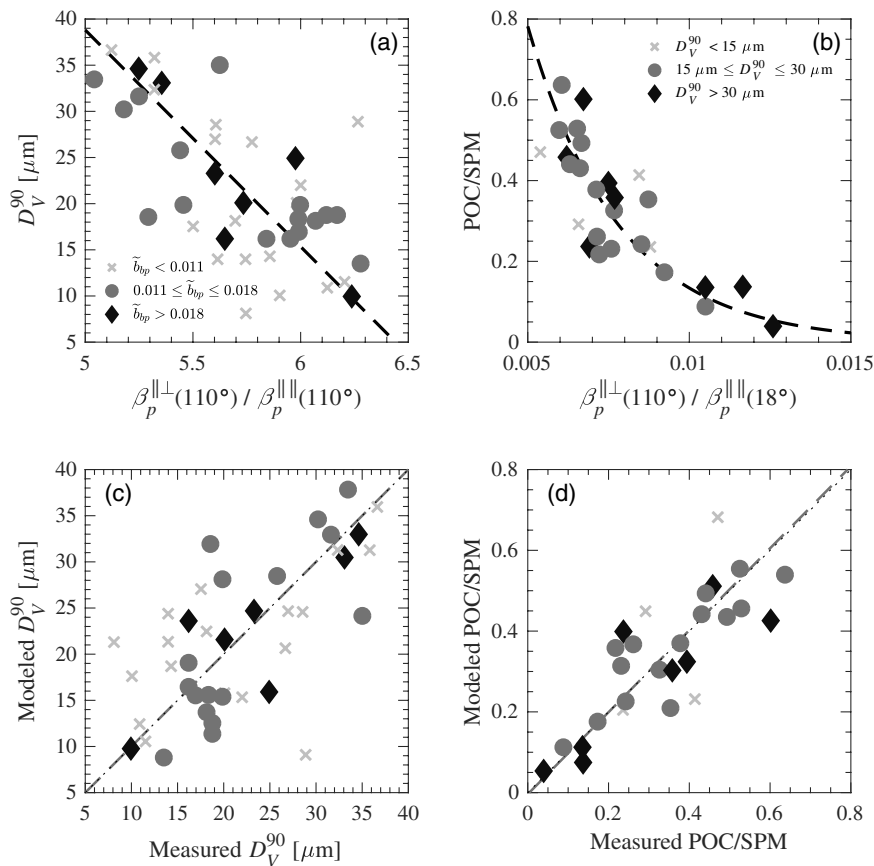

Fig. 12. (a) Particle size parameter D_v^{90} and (b) particle composition parameter POC/SPM as functions of polarized light scattering metrics for seawater samples. Linear regression (a) and exponential regression (b) functions are plotted with black dashed lines. Bottom panels (c), (d) present model performance using model-derived values from regression from the panel above and the measured D_v^{90} or POC/SPM, respectively. A type II linear regression of modeled versus measured data is plotted with a gray dashed line. A 1:1 dotted line is also plotted, which is nearly indistinguishable from the regression line. Data in (a), (c) are indicated by particulate composition-related parameter $\tilde{b}_{bp}$ as shown in legend in (a), while (b), (d) are indicated by particle size parameter D_v^{90} as shown in legend in (b).

for POC/SPM versus $\beta_p^{\parallel\perp}(110°)/\beta_p^{\parallel\parallel}(18°)$. This comparison suggests that $\beta_p^{\parallel\perp}(110°)/\beta_p^{\parallel\parallel}(18°)$ provides a somewhat better proxy of POC/SPM than $\tilde{b}_{bp}$.

Summarizing the results in Fig. 12, we note that in the case of estimating particle size, normalizing $\beta_p^{\parallel\perp}(110°)$ by $\beta_p^{\parallel\parallel}(110°)$ results in a measurement that correlates well with D_v^{90}, with no

clear influence of particle composition as parameterized by $\tilde{b}_{bp}$. For the case of estimating particle composition, normalizing $\beta_p^{\parallel\perp}(110°)$ by $\beta_p^{\parallel\parallel}(18°)$ results in a measurement that correlates well with POC/SPM, with no clear influence of PSD as parametrized by D_v^{90}. None of the chosen proxies presented earlier in this section change if the angular range of the analysis is expanded to include $\psi_1 = 121° - 150°$.

4. SUMMARY AND CONCLUDING REMARKS

The current study involved 16 seawater samples representing contrasting natural assemblages of particles from coastal environments. Each sample underwent comprehensive characterization in terms of angle-resolved polarized light scattering, particle composition in terms of various metrics derived from particulate mass concentration and light absorption, and PSD. Samples were additionally characterized following particle-size fractionation with 5 µm and 20 µm mesh filters. Both the scattering parameters and the particle characteristics represent the bulk properties of highly heterogeneous polydisperse assemblages of natural aquatic particles.

We observed reductions of $\text{DoLP}_{p,\max}$ to be weakly dependent on particle composition and mainly associated with increased proportions of the relatively rare large-sized particles. Additionally, we found values of the scattering matrix element $p_{22}(20°)$ to be weakly dependent on particle size and range between about 0.92 and 1.0, with the lowest values associated with non-phytoplankton- or inorganic- dominated assemblages and the highest values associated with organic- or phytoplankton-dominated assemblages. On the other hand, values of $p_{22}(100°)$ were weakly dependent on particle composition and ranged between about 0.92 and 0.97, with the lowest values generally associated with particle assemblages containing higher proportions of large-sized particles, and the highest values associated with lower proportions of large-sized particles.

Other polarization-based parameters were also examined as potential proxies to estimate particle size (D_v^{90}) and composition (POC/SPM) characteristics from scattering measurements at only one or two angles. We identified two polarization parameters, namely, $\beta_p^{\parallel\perp}(110°)/\beta_p^{\parallel\parallel}(110°)$ and $\beta_p^{\parallel\perp}(110°)/\beta_p^{\parallel\parallel}(18°)$, as most suitable proxies for estimating D_v^{90} and POC/SPM, respectively. Note that these parameters share the polarization measurement combination of $\beta_p^{\parallel\perp}(\psi_1)$, with ψ_1 near 110°. Thus, a relatively simple optical approach based on three polarization measurements could provide a means to estimate D_v^{90} and POC/SPM. Our data suggest that such an approach could estimate both D_v^{90} and POC/SPM with MdAPD of about 20% and therefore provides useful characterization of the proportions of small- versus large-sized particles and organic versus inorganic particles with unprecedented efficiency offered by *in situ* optical measurements. At present, these types of particulate characterization are typically achieved following laborious lab-based analysis on discrete seawater samples, which significantly limits spatial and temporal scales of observations compared to *in situ* optical measurements.

The empirical relationships or linkages between light scattering and particle characteristics derived from concurrent measurements of the bulk inherent properties of polarized light scattering and bulk compositional and size characteristics of highly heterogeneous polydisperse assemblages of marine particle have special significance because even the most advanced or sophisticated models of light scattering by particles cannot adequately simulate the complexities of such particle assemblages. Therefore, it can be challenging to use theoretical models to explain or interpret observations from highly complex natural particle assemblages, so any attempt to compare our experimental results with modeling results requires a great deal of caution. The patterns seen in our experimental data reflect the net effect associated with the interplay of various particle characteristics within highly heterogeneous polydisperse assemblages of particles; for example, variations in the distribution of various particle types with associated refractive indices and shapes across a broad range of particle sizes, which are all important to polarized light scattering. Such complexity cannot be fully characterized or captured by models. We therefore expect that while some patterns observed in our relationships between the bulk scattering and particle characteristics may reveal clear correspondence with theoretical findings, others may at first glance appear counterintuitive in comparison with theoretical predictions. For example, the observed tendency for a decrease of measured $\text{DoLP}_{p,\max}$ with increasing proportion of large-sized particles (or equivalently decreasing proportion of small-size particles) is generally consistent with theoretical findings or laboratory measurements of individual particle types [17,6,43,50]. In contrast, we did not observe correlation of $\text{DoLP}_{p,\max}$ with compositional parameters within the examined range of POC/SPM in our data set, which at first glance could appear counterintuitive when considering the effects of refractive index shown through modeling results or measurements of individual particle types [14,16,51]. We believe, however, that there is no inconsistency between these results because our experimental data reflect a much more complex interplay of multiple physical and chemical properties of particles within heterogeneous polydisperse assemblages compared to modeling assumptions of particle properties or measurements on individual particle types. Another example is the potential challenge in using results of modeling studies for interpreting our measurements of $p_{22}(\psi)$ of seawater samples. Our measurements were made on highly complex assemblages of particles, which were most likely in random orientation, and the resulting $p_{22}(\psi)$ values do not differ much from 1, which is generally known to represent spherical particles. Theoretical studies showed, for example, that small deviations from 1 can be accounted for by significant nonsphericity of particles when refractive index is close to that of water [52], by aggregation of spherical particles [44], and by increases in refractive index or changes in the effective size parameter of randomly oriented spheroids [43,51]. In the discussion of our data we generally refrained from detailed comparisons with theoretical models and focused on linkages between the measured bulk scattering parameters and particle compositional and size proxies, such as POC/SPM and D_v^{90}, while acknowledging that these proxies also have some limitations; for example, the particle size range included in our measurements does not encompass all particles contributing to scattering.

Whereas the relationships presented in the current study have the potential to pave the way for increased interest in and significant use of polarized light scattering measurements in aquatic sciences, further research on samples from diverse marine environments with enhanced measurement capabilities, especially in terms of particle size characterization, are needed. The present relationships were developed with relatively small number of samples, and although a broad range of aquatic particulate assemblages were included, some types of environments, such as oligotrophic open-ocean waters, are not represented in our data set. The other limitation of our study is that the PSD measurements were limited to the particle size range of 2–60 µm, and therefore populations of particles outside this range have not been included in the size parameter D_v^{90}. Comprehensive experiments, similar to that described in this paper, will be needed in diverse environments to further investigate and validate the potential usefulness of polarization-based proxies derived from measurements of the inherent polarization scattering properties to characterize particle size and composition. In addition, such experiments will enhance fundamental knowledge about the inherent polarization scattering properties of marine particle assemblages, which will aid in advancing the applications associated with polarimetric measurements of oceanic light fields, including the applications associated with remote-sensing of water-leaving light. Such advancements are needed in view of recent increased efforts to include polarimetric measurements above water [53], including airborne [54], ship-based LIDAR [55], and satellite observations of the ocean, e.g., the NASA Plankton, Aerosol, Cloud ocean Ecosystem (PACE) mission expected to launch in 2022 [56,57].

Disclosures. The authors declare no conflicts of interest.

REFERENCES

1. C. F. Bohren and D. R. Huffman, *Absorption and Scattering of Light by Small Particles* (Wiley, 1983).
2. P. A. Yanamandra-Fisher and M. S. Hanner, "Optical properties of nonspherical particles of size comparable to the wavelength of light: application to comet dust," Icarus **138**, 107–128 (1999).
3. M. I. Mishchenko, J. W. Hovenier, and L. D. Travis, *Light Scattering by Nonspherical Particles: Theory, Measurements, and Applications* (Academic, 2000).
4. O. Muñoz, F. Moreno, D. Guirado, D. D. Dabrowska, H. Volten, and J. W. Hovenier, "The Amsterdam–Granada light scattering database," J. Quant. Spectrosc. Radiat. Transf. **113**, 565–574 (2012).
5. E. Zubko, "Light scattering by irregularly shaped particles with sizes comparable to the wavelength," in *Light Scattering Reviews 6*, A. A. Kokhanovsky, ed. (Springer, 2012), pp. 39–74.
6. H. Volten, O. Muñoz, E. Rol, J. D. Haan, W. Vassen, J. W. Hovenier, and T. Nousiainen, "Scattering matrices of mineral aerosol particles at 441.6 nm and 632.8 nm," J. Geophys. Res. **106**, 17375–17401 (2001).
7. O. Dubovik, Z. Li, M. I. Mishchenko, D. Tanré, Y. Karol, B. Bojkov, B. Cairns, D. J. Diner, W. R. Espinosa, P. Goloub, X. Gu, O. Hasekamp, J. Hong, W. Hou, K. D. Knobelspiesse, J. Landgraf, L. Li, P. Litvinov, Y. Liu, A. Lopatin, T. Marbach, H. Maring, V. Martins, Y. Meijer, G. Milinevsky, S. Mukai, F. Parol, Y. Qiao, L. Remer, J. Rietjens, I. Sano, P. Stammes, S. Stamnes, X. Sun, P. Tabary, L. D. Travis, F. Waquet, F. Xu, C. Yan, and D. Yin, "Polarimetric remote sensing of atmospheric aerosols: instruments, methodologies, results, and perspectives," J. Quant. Spectrosc. Radiat. Transf. **224**, 474–511 (2019).
8. M. Chami, "Importance of the polarization in the retrieval of oceanic constituents from the remote sensing reflectance," J. Geophys. Res. **112**, C05026 (2007).
9. H. Loisel, L. Duforet, D. Dessailly, M. Chami, and P. Dubuisson, "Investigation of the variations in the water leaving polarized reflectance from the POLDER satellite data over two biogeochemical contrasted oceanic areas," Opt. Express **16**, 12905–12918 (2008).
10. A. Ibrahim, A. Gilerson, J. Chowdhary, and S. Ahmed, "Retrieval of macro- and micro-physical properties of oceanic hydrosols from polarimetric observations," Remote Sens. Environ. **186**, 548–566 (2016).
11. E. S. Fry and K. J. Voss, "Measurement of the Mueller matrix for phytoplankton," Limnol. Oceanogr. **30**, 1322–1326 (1985).
12. M. S. Quinby-Hunt, A. J. Hunt, K. Lofftus, and D. Shapiro, "Polarized-light scattering studies of marine Chlorella," Limnol. Oceanogr. **34**, 1587–1600 (1989).
13. P. J. Wyatt and C. Jackson, "Discrimination of phytoplankton via light-scattering properties," Limnol. Oceanogr. **34**, 96–112 (1989).
14. H. Volten, J. F. De Haan, J. W. Hovenier, R. Schreurs, W. Vassen, A. G. Dekker, H. J. Hoogenboom, F. Charlton, and R. Wouts, "Laboratory measurements of angular distributions of light scattered by phytoplankton and silt," Limnol. Oceanogr. **43**, 1180–1197 (1998).
15. Ø. Svensen, J. J. Stamnes, M. Kildemo, L. M. S. Aas, S. R. Erga, and Ø. Frette, "Mueller matrix measurements of algae with different shape and size distributions," Appl. Opt. **50**, 5149–5157 (2011).
16. M. Chami, A. Thirouard, and T. Harmel, "POLVSM (Polarized Volume Scattering Meter) instrument: an innovative device to measure the directional and polarized scattering properties of hydrosols," Opt. Express **22**, 26403–26428 (2014).
17. T. Hatch and S. P. Choate, "Measurement of polarization of the Tyndall beam of aqueous suspension as an aid in determining particle size," J. Franklin Inst. **210**, 793–804 (1930).
18. D. Stramski, E. S. Boss, D. J. Bogucki, and K. J. Voss, "The role of seawater constituents in light backscattering in the ocean," Prog. Oceanogr. **61**, 27–56 (2004).
19. G. F. Beardsley, "Mueller scattering matrix of sea water," J. Opt. Soc. Am. **58**, 52–57 (1968).
20. Y. A. Kadyshevich, "Light-scattering matrices of inshore waters of the Baltic Sea," Izv. Acad. Sci. USSR Atmos. Ocean. Phys. **13**, 77–78 (1977).
21. K. J. Voss and E. S. Fry, "Measurement of the Mueller matrix for ocean water," Appl. Opt. **23**, 4427–4439 (1984).
22. W. S. Bickel and W. M. Bailey, "Stokes vectors, Mueller matrices, and polarized scattered light," Am. J. Phys. **53**, 468–478 (1985).
23. J. W. Hovenier, H. Volten, O. Muñoz, W. J. Van der Zande, and L. B. F. M. Waters, "Laboratory studies of scattering matrices for randomly oriented particles: potentials, problems, and perspectives," J. Quant. Spectrosc. Radiat. Transf. **79**, 741–755 (2002).
24. A. A. Kokhanovsky, "Parameterization of the Mueller matrix of oceanic waters," J. Geophys. Res. **108**, 3175 (2003).
25. D. Koestner, D. Stramski, and R. A. Reynolds, "Measurements of the volume scattering function and the degree of linear polarization of light scattered by contrasting natural assemblages of marine particles," Appl. Sci. **8**, 2690 (2018).

26. M. Jonasz and G. Fournier, *Light Scattering by Particles in Water: Theoretical and Experimental Foundations* (Elsevier, 2007).

27. D. Koestner, D. Stramski, and R. A. Reynolds, "Assessing the effects of particle size and composition on light scattering through measurements of size-fractionated seawater samples," Limnol. Oceanogr. **65**, 173–190 (2020).

28. D. W. van der Linde, "Protocol for the determination of total suspended matter in oceans and coastal zones," Technical Note I.98.182 (Joint Research Centre, 1998).

29. T. R. Parsons, Y. Maita, and C. M. Lalli, *A Manual of Chemical and Biological Methods for Seawater Analysis* (Elsevier, 1984).

30. R. J. Ritchie, "Universal chlorophyll equations for estimating chlorophylls a, b, c, and d and total chlorophylls in natural assemblages of photosynthetic organisms using acetone, methanol, or ethanol solvents," Photosynthetica **46**, 115–126 (2008).

31. S. B. Woźniak, D. Stramski, M. Stramska, R. A. Reynolds, V. M. Wright, E. Y. Miksic, M. Cichocka, and A. M. Cieplak, "Optical variability of seawater in relation to particle concentration, composition, and size distribution in the nearshore marine environment at Imperial Beach, California," J. Geophys. Res. **115**, C08027 (2010).

32. R. Röttgers and S. Gehnke, "Measurement of light absorption by aquatic particles: improvement of the quantitative filter technique by use of an integrating sphere approach," Appl. Opt. **51**, 1336–1351 (2012).

33. D. Stramski, R. A. Reynolds, S. Kaczmarek, J. Uitz, and G. Zheng, "Correction of pathlength amplification in the filter-pad technique for measurements of particulate absorption coefficient in the visible spectral region," Appl. Opt. **54**, 6763–6782 (2015).

34. M. Kishino, M. Takahashi, N. Okami, and S. Ichimura, "Estimation of the spectral absorption coefficients of phytoplankton in the sea," Bull. Mar. Sci. **37**, 634–642 (1985).

35. H. C. van de Hulst, *Light Scattering by Small Particles* (Wiley, 1981).

36. M. I. Mishchenko and L. D. Travis, "Light scattering by polydisperse, rotationally symmetric nonspherical particles: linear polarization," J. Quant. Spectrosc. Radiat. Transf. **51**, 759–778 (1994).

37. *LISST-VSF Multi-Angle Polarized Light Scattering Meter: User's Manual Revision A* (Sequoia Scientific, 2013).

38. J. W. Hovenier, H. C. van de Hulst, and C. V. M. van der Mee, "Conditions for the elements of the scattering matrix," Astron. Astrophys. **157**, 301–310 (1985).

39. W. E. Ricker, "Linear regressions in fishery research," J. Fish. Res. Board Can. **30**, 409–434 (1973).

40. R. R. Sokal and F. J. Rohlf, *Biometry: The Principles and Practice of Statistics in Biological Research*, 3rd ed. (W. H. Freeman, 1995).

41. D. G. Altman and J. M. Bland, "Measurement in medicine: the analysis of method comparison studies," Statistician **32**, 307–317 (1983).

42. J. M. Bland and D. G. Altman, "Statistical method for assessing agreement between two methods of clinical measurement," Lancet **327**, 307–310 (1983).

43. M. I. Mishchenko and L. D. Travis, "Light scattering by polydispersions of randomly oriented spheroids with sizes comparable to wavelengths of observation," Appl. Opt. **33**, 7206–7225 (1994).

44. M. I. Mishchenko, L. D. Travis, and D. W. Mackowski, "T-Matrix computations of light scattering by nonspherical particles: a review," J. Quant. Spectrosc. Radiat. Transf. **55**, 535–575 (1996).

45. D. Stramski, A. Bricaud, and A. Morel, "Modeling the inherent optical properties of the ocean based on the detailed composition of planktonic community," Appl. Opt. **40**, 2929–2945 (2001).

46. M. S. Twardowski, E. Boss, J. B. Macdonald, W. S. Pegau, A. H. Barnard, and J. R. V. Zaneveld, "A model for estimating bulk refractive index from the optical backscattering ratio and the implications for understanding particle composition in case I and case II waters," J. Geophys. Res. **106**, 14129–14142 (2001).

47. E. Boss, W. S. Pegau, M. Lee, M. Twardowski, E. Shybanov, G. Korotaev, and F. Baratange, "Particulate backscattering ratio at LEO 15 and its use to study particle composition and distribution," J. Geophys. Res. **109**, C01014 (2004).

48. A. Morel and A. Bricaud, "Inherent optical properties of algal cells including picoplankton: theoretical and experimental results," Can. Bull. Fish. Aquat. Sci. **214**, 521–559 (1986).

49. A. Quirantes, F. Arroyo, and J. Quirantes-Ros, "Multiple light scattering by spherical particle systems and its dependence on concentration: a T-Matrix study," J. Colloid Interface Sci. **240**, 78–82 (2001).

50. D. Petrov, E. Synelnyk, Y. Shkuratov, and G. Videen, "The T-matrix technique for calculations of scattering properties of ensembles of randomly oriented particles with different size," J. Quant. Spectrosc. Radiat. Transf. **102**, 85–110 (2006).

51. J. K. Lotsberg and J. J. Stamnes, "Impact of particulate oceanic composition on the radiance and polarization of underwater and backscattered light," Opt. Express **18**, 10432–10445 (2010).

52. B. Sun, G. W. Kattawar, P. Yang, M. S. Twardowski, and J. M. Sullivan, "Simulation of the scattering properties of a chain-forming triangular prism oceanic diatom," J. Quant. Spectrosc. Radiat. Transf. **178**, 390–399 (2016).

53. A. Gilerson, C. Carrizo, A. Ibrahim, R. Foster, T. Harmel, A. El-Habashi, Z. Lee, X. Yu, S. Ladner, and M. Ondrusek, "Hyperspectral polarimetric imaging of the water surface and retrieval of water optical parameters from multi-angular polarimetric data," Appl. Opt. **59**, C8–C20 (2020).

54. J. H. Bowles, D. R. Korwan, M. J. Montes, D. J. Gray, D. B. Gillis, G. M. Lamela, and W. D. Miller, "Airborne system for multispectral, multiangle polarimetric imaging," Appl. Opt. **54**, F256–F267 (2015).

55. B. L. Collister, R. C. Zimmerman, V. J. Hill, C. I. Sukenik, and W. M. Balch, "Polarized lidar and ocean particles: insights from a mesoscale coccolithophore bloom," Appl. Opt. **59**, 4650–4662 (2020).

56. P. J. Werdell, M. J. Behrenfeld, P. S. Bontempi, E. Boss, B. Cairns, G. T. Davis, B. A. Franz, U. B. Gliese, E. T. Gorman, O. Hasekamp, K. D. Knobelspiesse, A. Mannino, J. V. Martins, C. R. McClain, G. Meister, and L. Remer, "The Plankton, Aerosol, Cloud, ocean Ecosystem (PACE) mission: status, science, advances," Bull. Am. Meteorol. Soc. **100**, 1775–1794 (2019).

57. O. P. Hasekamp, G. Fu, S. P. Rusli, L. Wu, A. D. Noia, J. aan de Brugh, J. Landgraf, J. M. Smit, J. Rietjens, and A. van Amerongen, "Aerosol measurements by SPEXone on the NASA PACE mission: expected retrieval capabilities," J. Quant. Spectrosc. Radiat. Transf. **227**, 170–184 (2019).